Supporting Information

Plasmon induced hot electron generation in two dimensional carbonaceous nanosheets decorated with Au nanostars: Enhanced photocatalytic activity under visible light

Ajay Kumar, Priyanka Choudhary, Kamlesh Kumar, Ashish Kumar and Venkata Krishnan*

School of Basic Sciences and Advanced Materials Research Center, Indian Institute of Technology Mandi, Kamand, Mandi 175075, Himachal Pradesh, India.

Email: vkn@iitmandi.ac.in

S1 Materials characterization

The zeta potential measurements of colloidal suspension were performed using Zeta sizer Nano ZS90, Malvern Instrument at room temperature. For this measurement, 1 mg mL^{-1} solutions were sonicated for 30 min to prepare disperse solution and then pH was adjusted from 2 to 12 before measurement. X-ray diffraction (XRD) measurements were done using the Rigaku Smart Lab 9 kW rotating anode x-ray diffractometer with Ni-filtered Cu K_α irradiation (λ = 0.1542 nm) at 45 kV and 100 mA. The scans were done between 5° and 80°, with a scan step of 0.02° and an acquisition time of 1s. FTIR spectra were acquired on a PerkinElmer Spectrum 2 spectrometer. Thermogravimetric analysis (TGA) was carried out by using a PerkinElmer Pyris 1 instrument, wherein the samples were heated from room temperature to 800 °C at a heating rate of 10 °C min^{-1} under nitrogen atmosphere with a flow rate of 20 mL min^{-1}. The UV-visible absorption spectra of the samples were recorded using Shimadzu UV-2450 spectrophotometer in the wavelength range of 200 nm to 800 nm by dispersing all samples in deionized water. Morphological analysis of the nanocomposites was performed by using a field emission scanning electron microscope (FESEM), FEI Nova Nano SEM-450, and transmission electron microscope (TEM), FEI Tecnai G2 20 S-twin microscope operating at 200 kV. Energy dispersive x-ray spectra (EDAX) were obtained using the same TEM instruments. Atomic force microscopy (AFM) images were performed in tapping mode at a scanning rate of 0.9 Hz using a Dimension Icon, Bruker model.

The x-ray photoelectron spectroscopy (XPS) measurements were performed using NEXSA instrument, wherein the x-ray source was Al K-alpha and the energy was 1486.68 eV. The pass energy of the analyzer was 200 eV for acquiring survey scans and was 20 eV for the narrow scans. The data obtained from the instrument were processed and deconvoluted using Avantage software. Optical properties were analyzed by ultraviolet-visible (UV-vis) diffuse reflectance spectroscopy (DRS) using Perkin Elmer UV-vis-NIR Lambda 750 spectrophotometer in which polytetrafloroethylene (PTFE) polymer was employed as internal reflectance standard. The Brunauer–Emmett–Teller (BET) surface areas and nitrogen adsorption–desorption isotherms were measured at 77 K on Quantachrome Autosorb-iQMP-XR system, while the photoluminescence (PL) spectra were recorded on Agilent Technologies Cary Eclipse fluorescence spectrometer. NMR spectra were recorded on a JEOL 500 MHz spectrometer (JNMECX500) in DMSO-d_6 taking TMS (tetramethylsilane) as an internal standard. The ^{1}H-NMR and ^{13}C-NMR chemical shifts were reported in ppm relative to 2.50 and

39.5 ppm for DMSO-d_6. All ^{1}H-NMR spectra in DMSO-d_6 were recorded at 500 MHz frequency, and all ^{13}C-NMR spectra were recorded at 125 MHz frequency. High resolution mass spectra were recorded on an advance Bruker Daltonics (impact HD) UHR-QqTOF (ultra-high resolution Qq time-of-flight) mass spectrometer.

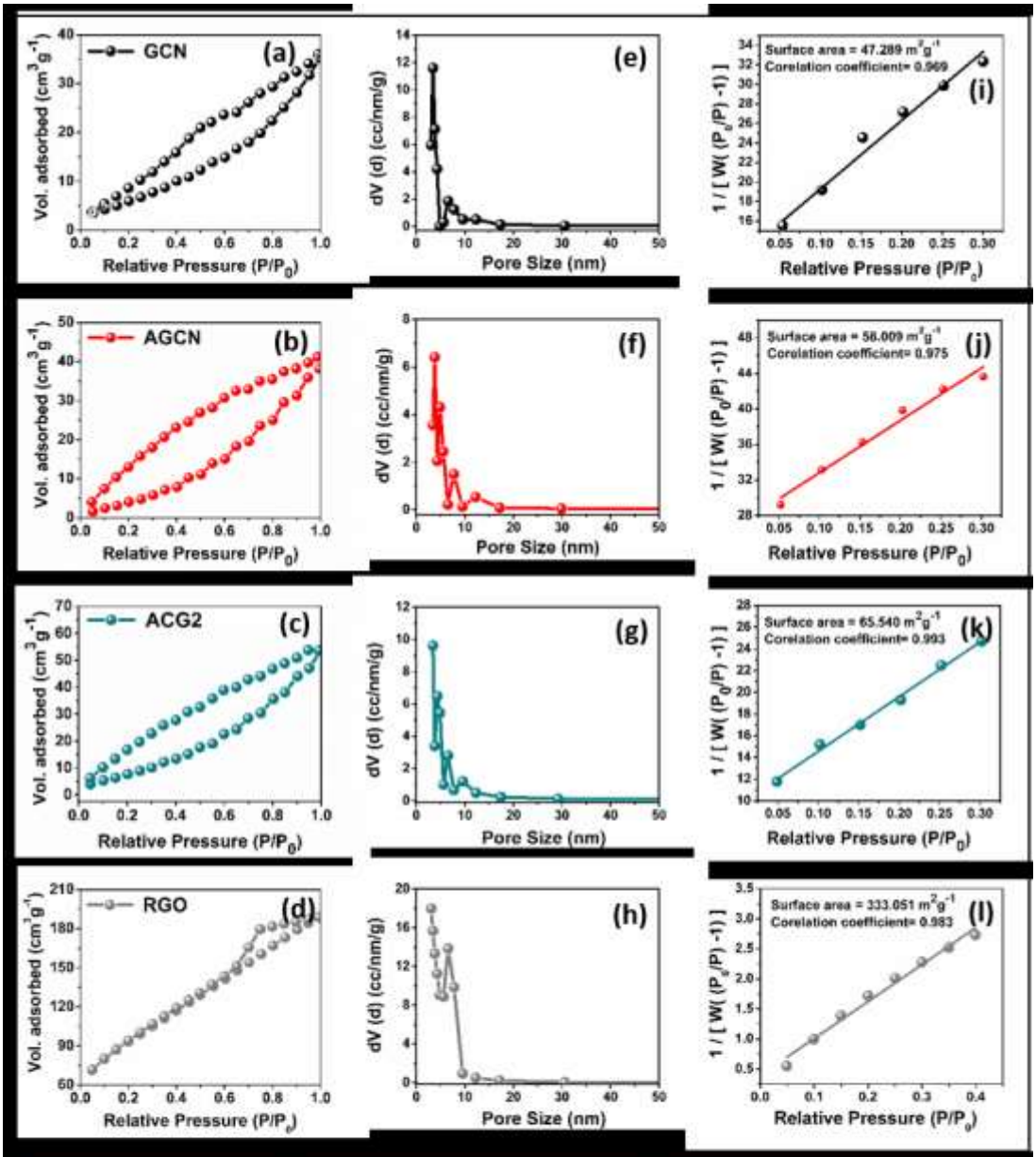

Sample	S_{BET} ($m^2 g^{-1}$)	Pore volume (cc g^{-1})
GCN	47.298	0.055
AGCN	58.009	0.042
ACG2	65.540	0.061
RGO	333.051	0.049

Fig. S1 (a-d) N_2 adsorption-desorption isotherms of GCN, AGCN, ACG2 and RGO (e-h) Pore size distribution curves for GCN, AGCN, ACG2 and RGO, (i-l) Linear fit curve from N_2 adsorption data for GCN, AGCN, ACG2 and RGO, respectively and summary of specific surface area and pore volume distribution of GCN, AGCN, AGC2 nanocomposite and RGO nanosheets.

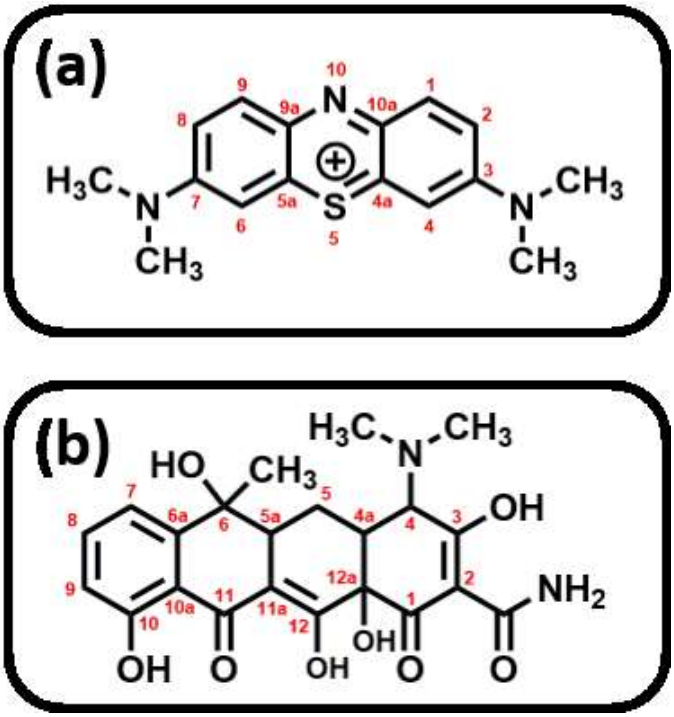

Fig. S2 Chemical structure of (a) methylene blue and (b) tetracycline molecules.

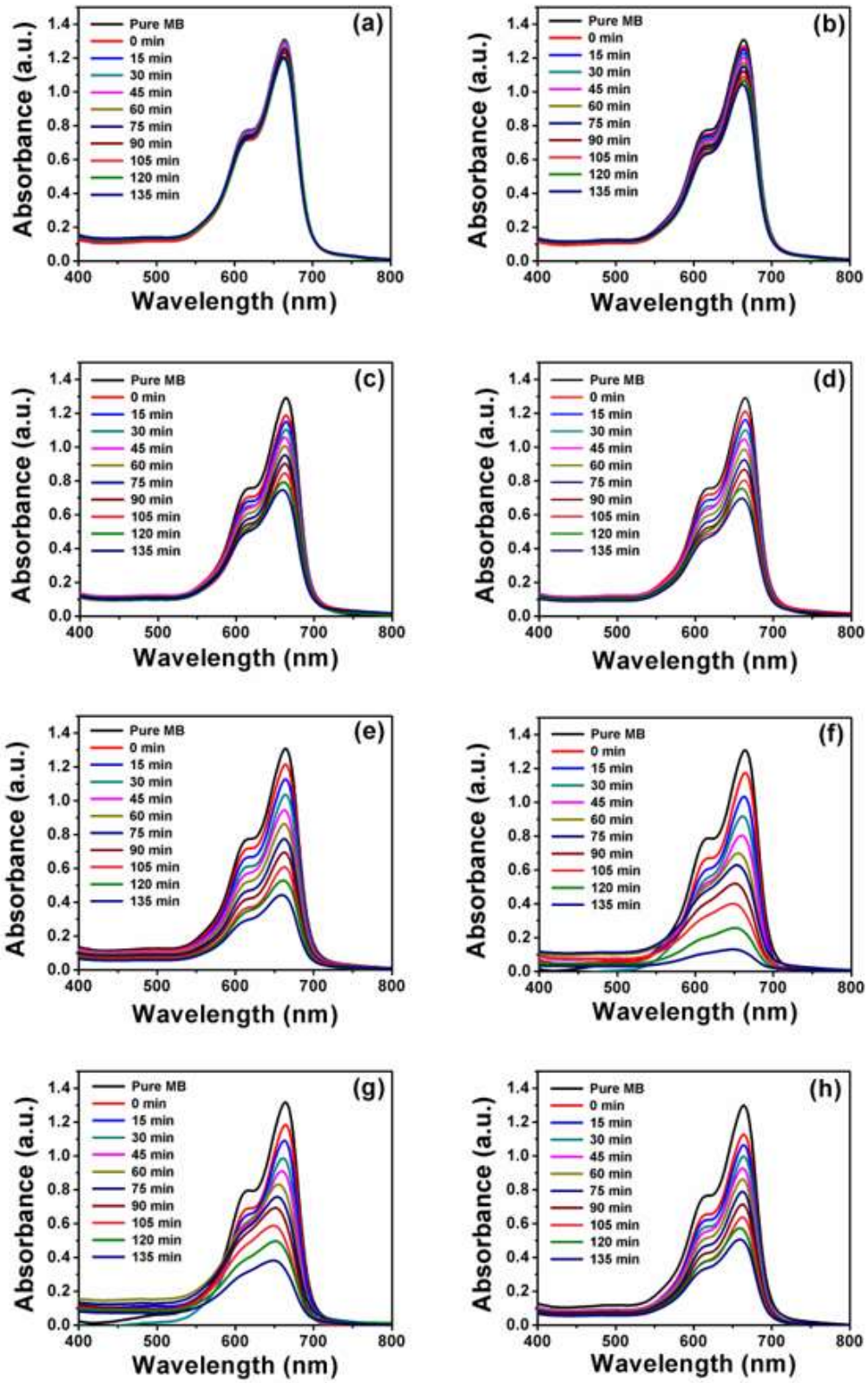

Fig. S3 Successive time dependent UV-vis spectra of photocatalytic degradation of MB under visible light irradiation (a) without catalyst, (b) GCN (c) CG2 (d) AGCN (e) ACG1 (f) ACG2 (g) ACG3 and (h) ACG5 nanocomposites.

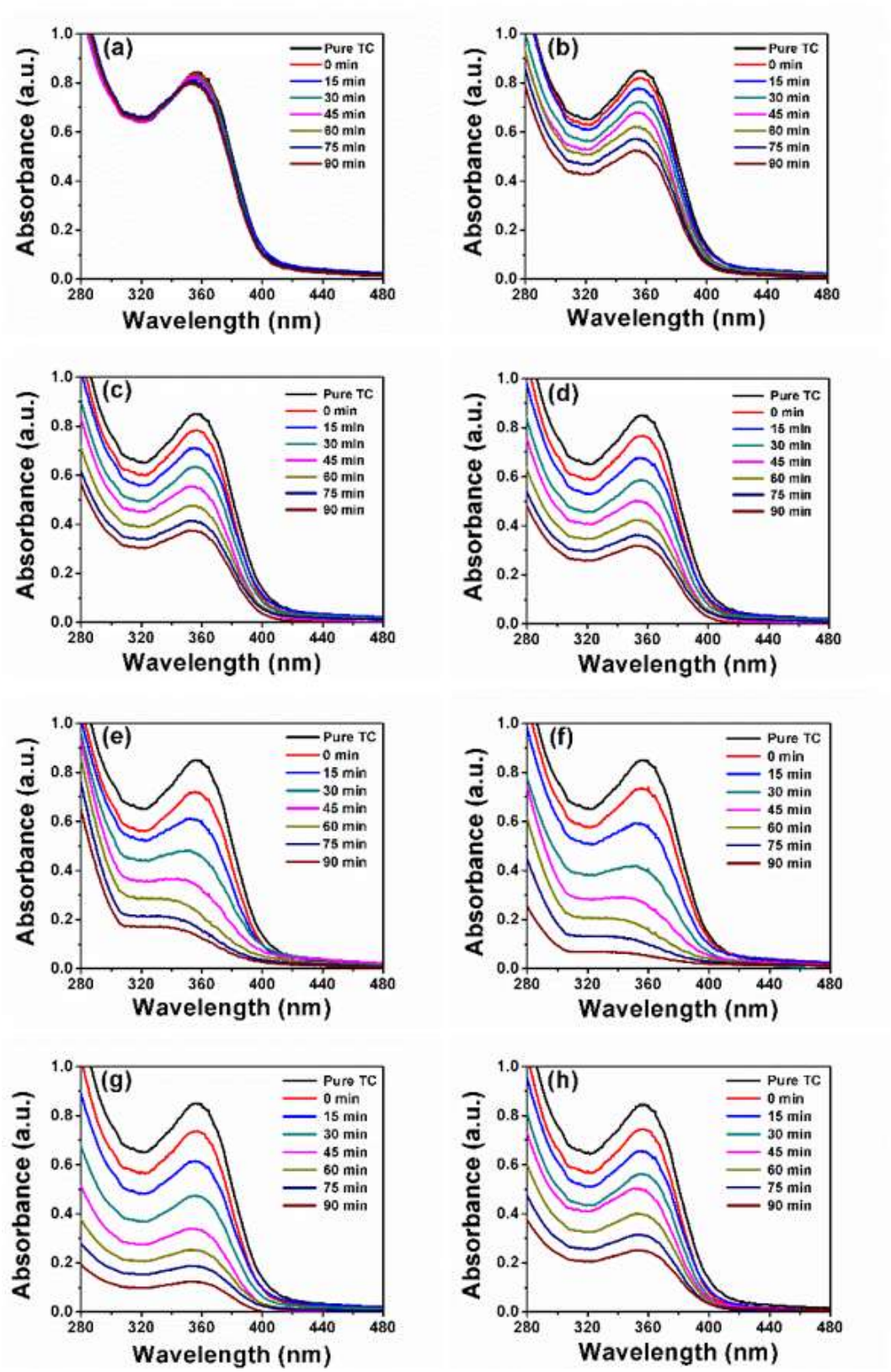

Fig. S4 Successive time dependent UV-vis spectra of photocatalytic degradation of TC under visible light irradiation (a) without catalyst, (b) GCN (c) CG2 (d) AGCN (e) ACG1 (f) ACG2 (g) ACG3 and (h) ACG5 nanocomposites.

Table S1 Summary of kinetic data of photocatalytic degradation of MB using all prepared photocatalysts under visible light irradiation.

Model of reaction		**WC**	**GCN**	**CG2**	**AGCN**	**ACG1**	**ACG2**	**ACG3**	**ACG5**
Zero Order	R^2	0.903	0.995	0.997	0.998	0.994	0.990	0.993	0.993
Zero Order	$k\times10^{-3}$	0.8	1.7	3.5	3.8	5.5	7.8	6.2	5.0
Pseudo First	R^2	0.900	0.990	0.983	0.982	0.961	0.857	0.941	0.967
Pseudo First	$k\times10^{-3}$	0.6	1.4	3.5	3.9	6.7	14.1	8.4	5.9
Parabolic diffusion	R^2	0.782	0.954	0.958	0.973	0.988	0.992	0.956	0.966
Parabolic diffusion	$k\times10^{-3}$	2.2	8.0	17.1	22.4	24.7	27.4	27.2	23.2
Modified Freundlich	R^2	0.981	0.996	0.991	0.998	0.995	0.997	0.987	0.978
Modified Freundlich	$k\times10^{-3}$	0.1	5.6	10.6	12.3	18.4	20.9	19.7	16.3

Table S2 Summary of kinetic data of photocatalytic degradation of TC using all prepared photocatalysts under visible light irradiation.

Model of reaction		**WC**	**GCN**	**CG2**	**AGCN**	**ACG1**	**ACG2**	**ACG3**	**ACG5**
Zero Order	R^2	0.899	0.967	0.979	0.979	0.974	0.972	0.972	0.993
Zero Order	$k\times10^{-3}$	0.5	2.9	4.3	4.7	6.9	7.4	6.6	5.4
Pseudo First	R^2	0.988	0.990	0.983	0.982	0.961	0.857	0.941	0.977
Pseudo First	$k\times10^{-3}$	0.5	1.4	3.5	3.9	6.7	14.1	8.38	5.6
Parabolic diffusion	R^2	0.773	0.937	0.971	0.986	0.954	0.981	0.959	0.86
Parabolic diffusion	$k\times10^{-3}$	1.1	8.8	30.7	40.0	60.7	69.5	56.0	48.3
Modified Freundlich	R^2	0.976	0.997	0.991	0.994	0.987	0.990	0.987	0.991
Modified Freundlich	$k\times10^{-3}$	3.2	8.5	25.2	34.0	53.2	63.8	50.2	39.5

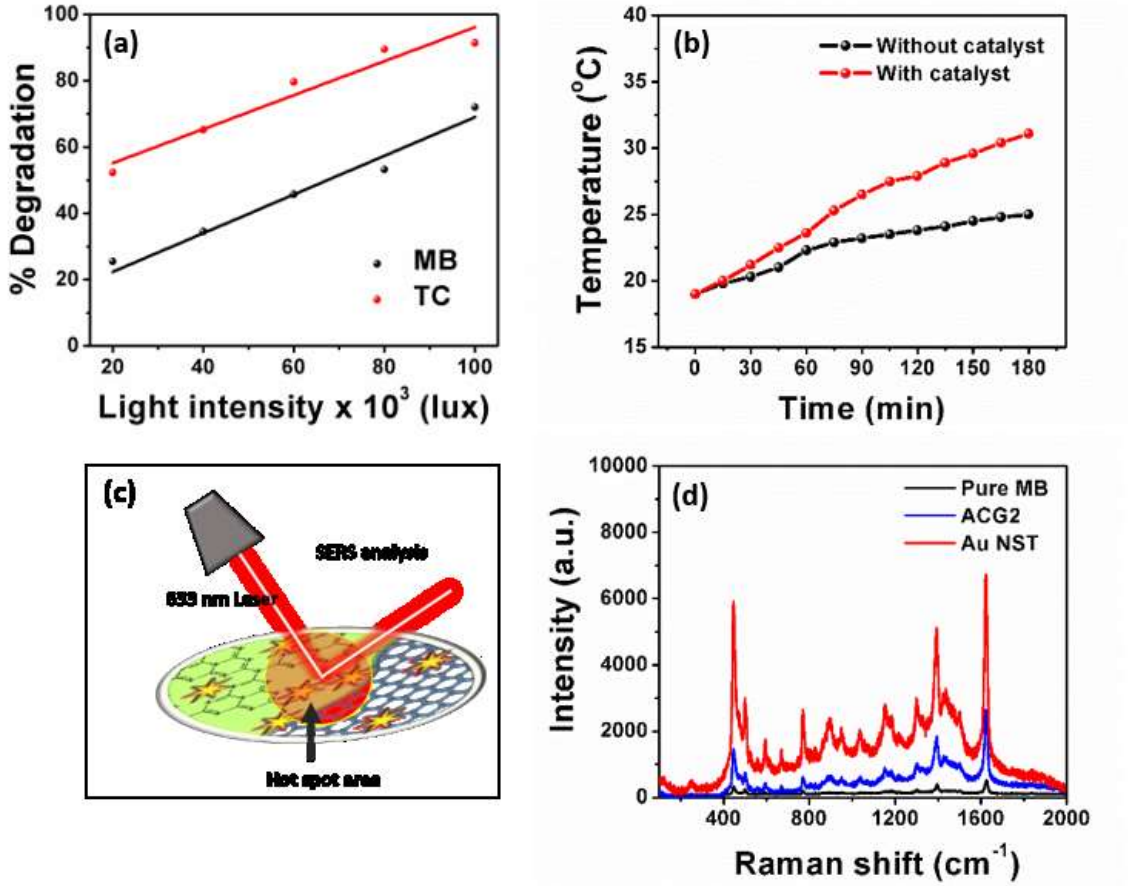

Fig. S5 (a) Light intensity dependent photocatalytic degradation of MB and TC monitored for a time period 60 min in each case, (b) rise in temperature of water with time under visible light illumination, (c) schematic of SERS process and (d) SERS spectra of MB in presence and absence of substrates.

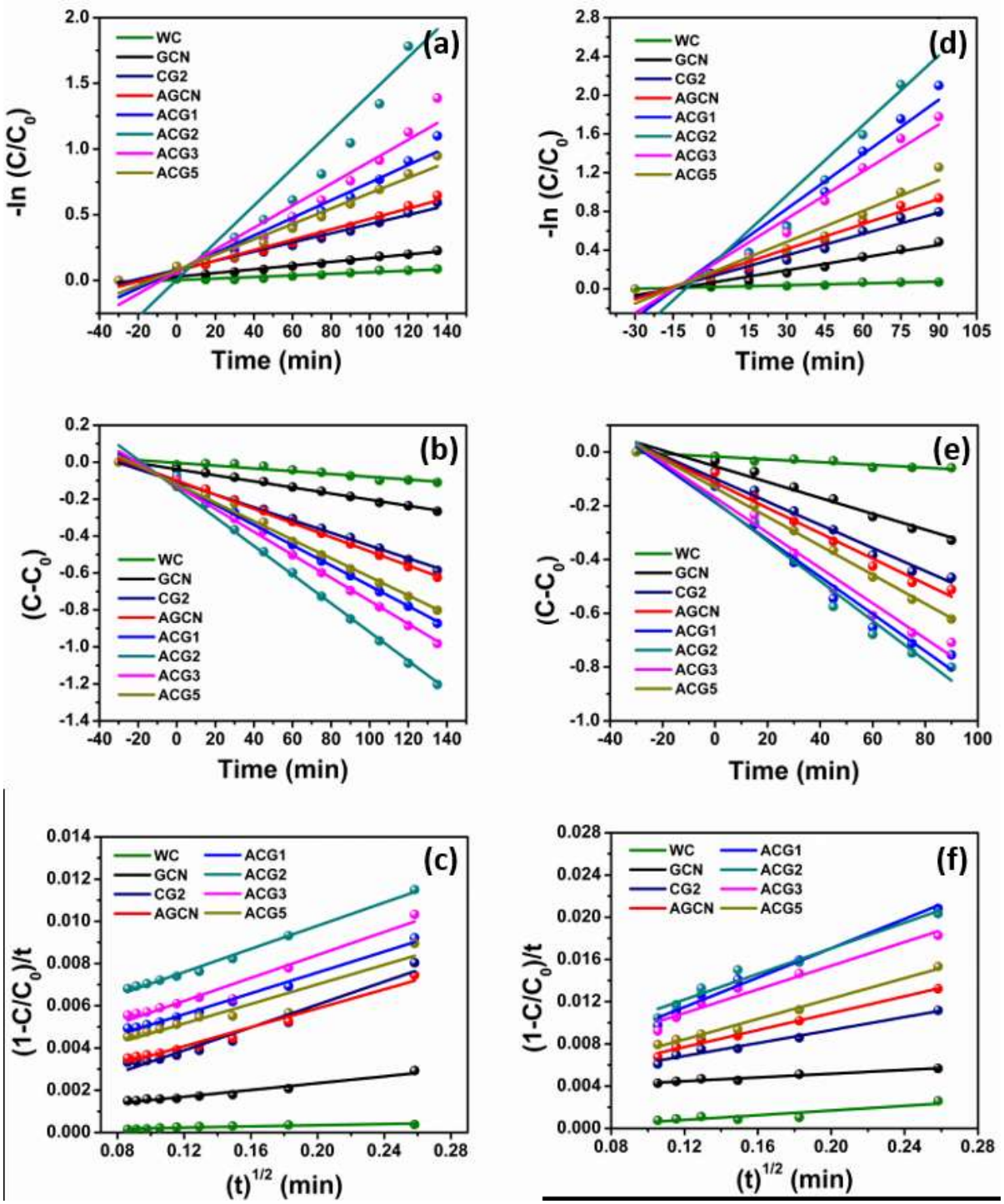

Fig. S6 Kinetics for the photocatalytic degradation of MB using (a) zero-order, (b) first-order, (c) parabolic diffusion models and TC using (a) zero-order, (b) first-order, (c) parabolic diffusion models under visible light irradiations.

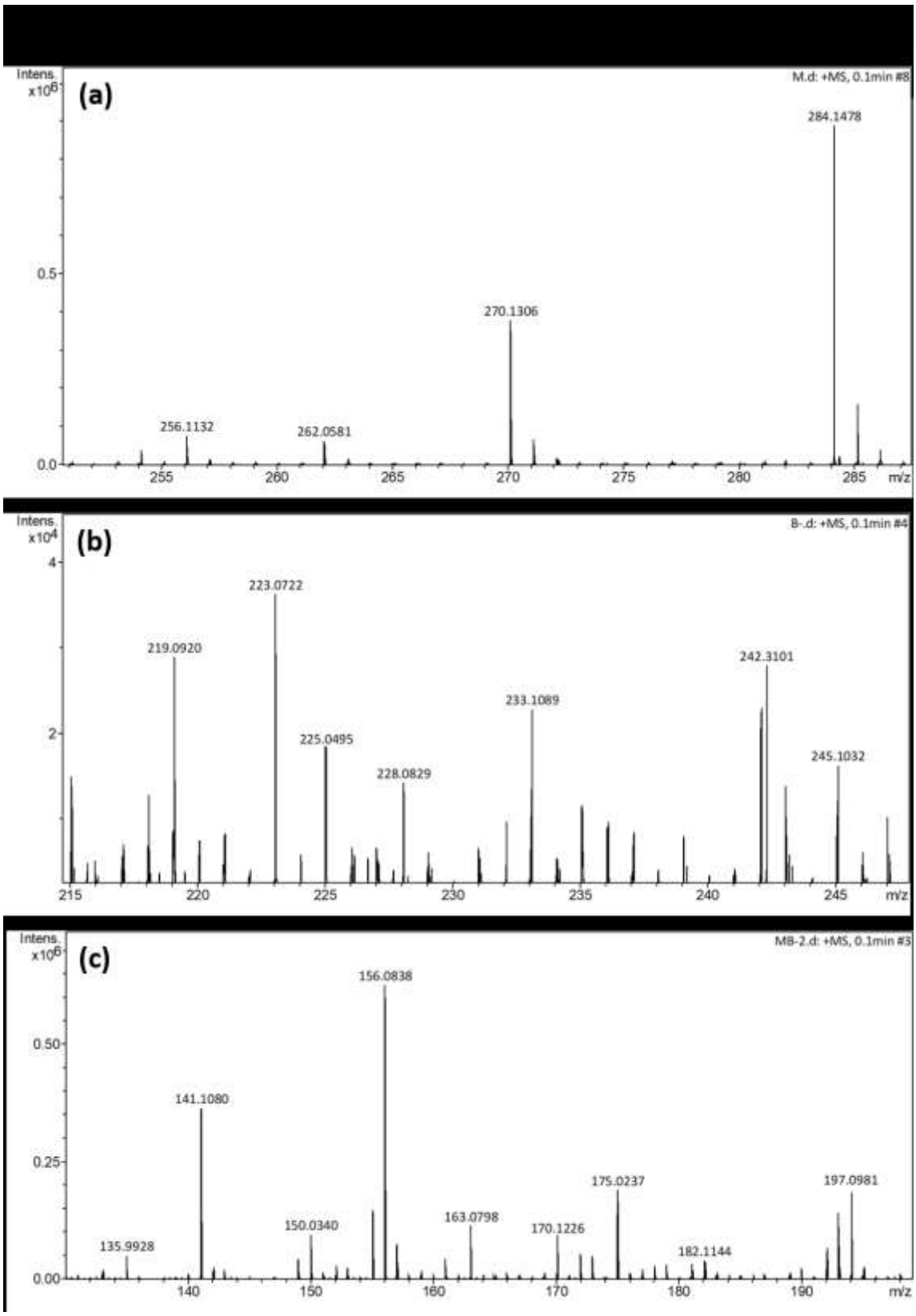

Fig. S7 Mass spectra of degradation of MB after visible light irradiation for 135 minutes.

Table S3 Summary of observed and calculated molecular masses of different fragments of MB obtained by mass analysis and their proposed molecular structures.

ID of intermediate	Molecular formula	m/z (observed)	m/z (calculated)	Molecular structure
MB	$C_{16}H_{18}N_3S^+$	284.12	284.15	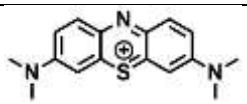
P1	$C_{16}H_{19}N_3S$	285.13	285.41	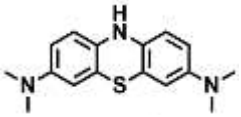
P2	$C_{15}H_{16}N_3S^+$	270.11	270.13	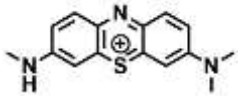
P3	$C_{14}H_{14}N_3S^+$	256.09	256.11	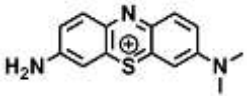
P4	$C_{13}H_{12}N_3S^+$	242.08	242.31	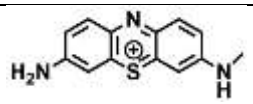
P5	$C_{12}H_{10}N_3S^+$	228.06	228.08	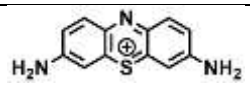
P6	$C_{10}H_{17}N_2S^+$	197.11	197.10	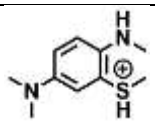
P7	$C_9H_{15}N_2S^+$	183.09	182.11	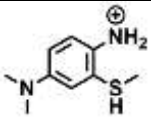
P8	$C_7H_{11}N_2S^+$	155.06	156.08	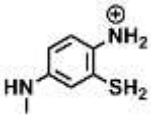
P9	$C_9H_{14}N_2$	150.12	150.03	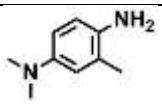
P10	$C_8H_{12}N_2$	136.10	135.99	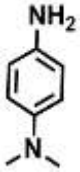

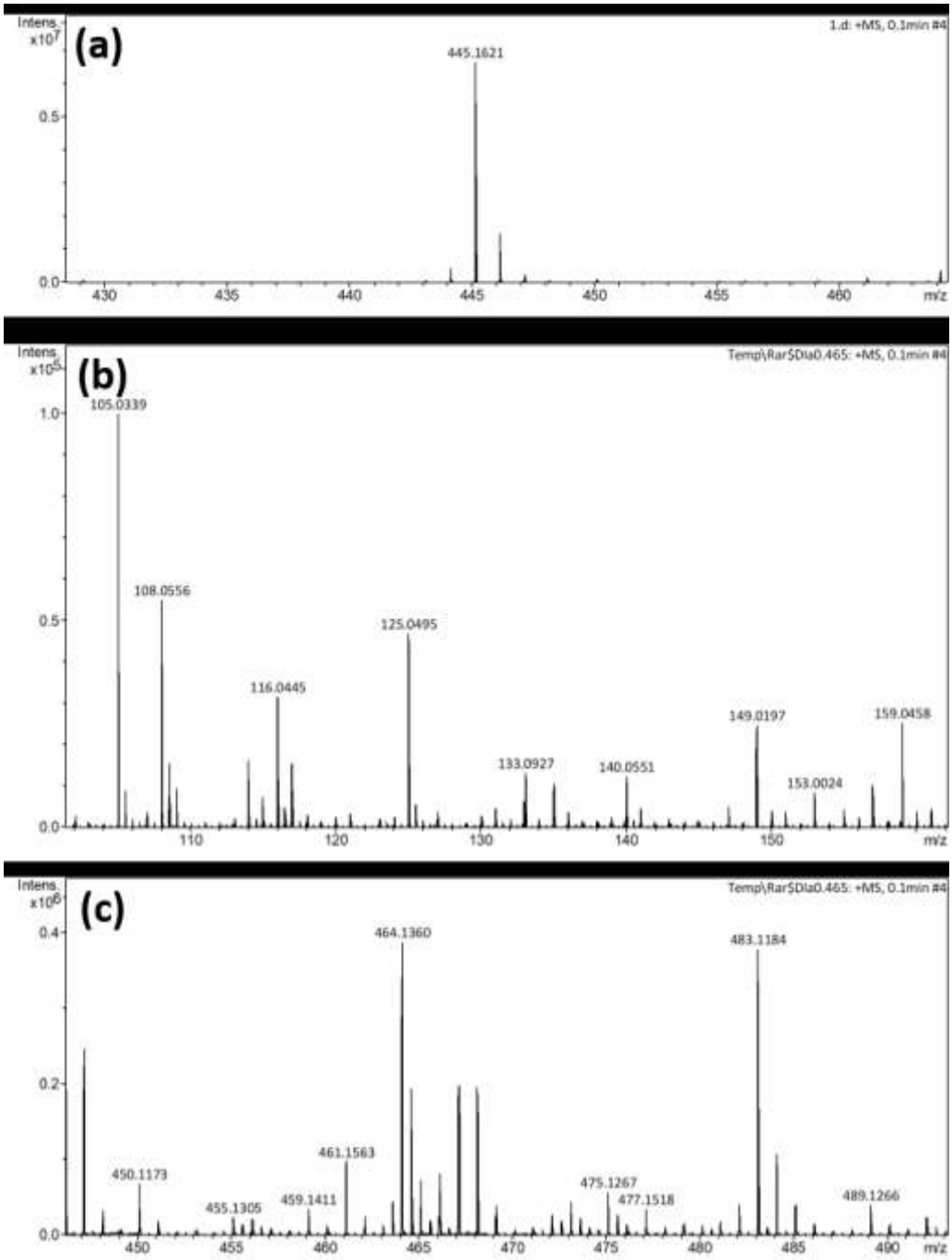

Fig. S8 Mass spectra of degradation of TC after visible light irradiation for 90 minutes.

Table S4 Summary of observed and calculated molecular masses of different fragments of TC obtained by mass analysis and their proposed molecular structures.

ID of intermediate	Molecular formula	m/z (observed)	m/z (calculated)	Molecular structure
TC	$C_{22}H_{24}N_2O_8$	445.16	444.15	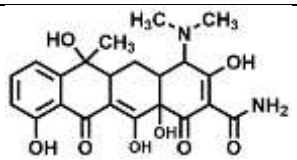
P'1	$C_{22}H_{24}N_2O_{10}$	477.15	476.14	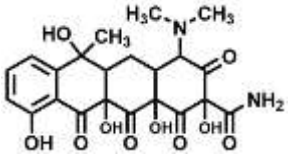
P'2	$C_{22}H_{22}N_2O_{11}$	489.12	490.12	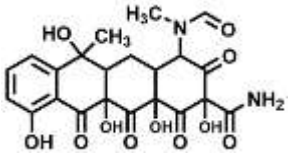
P'3	$C_{20}H_{20}N_2O_{10}$	448.16	448.11	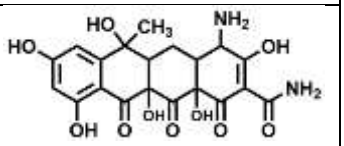
P'4	$C_{20}H_{20}N_2O_{10}$	450.11	450.12	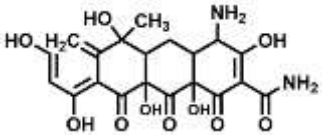
P'5	$C_9H_{12}O_2$	153.00	152.08	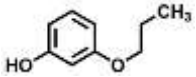
P'6	$C_9H_{10}O$	133.09	134.07	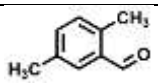
P'7	$C_4H_6O_4$	117.03	118.02	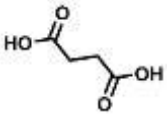
P'8	$C_4H_6O_5$	133.09	134.02	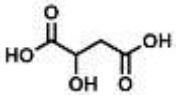
P'9	$C_3H_4O_4$	105.03	104.01	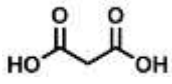
P'10	$C_2H_2O_4$	90.05	89.99	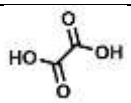

			Mean (mV)	Area (%)	St Dev (mV)
Zeta Potential (mV):	1.10	Peak 1:	1.10	100.0	3.60
Zeta Deviation (mV):	3.60	Peak 2:	0.00	0.0	0.00
Conductivity (mS/cm):	0.0459	Peak 3:	0.00	0.0	0.00
Result quality :	See result quality report				

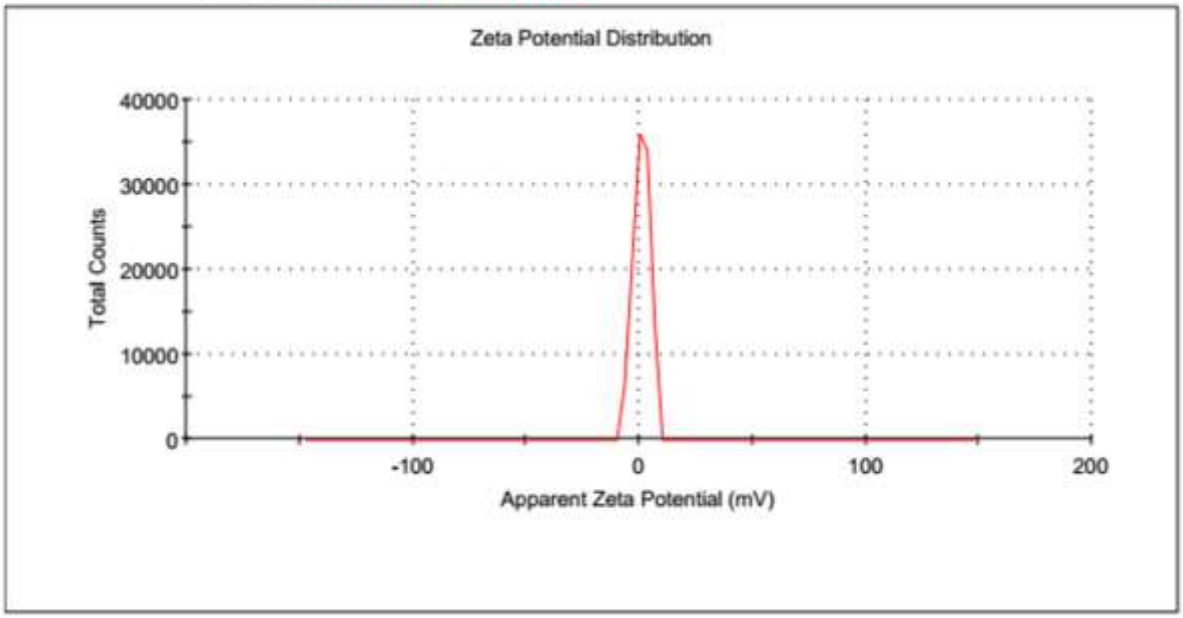

Fig. S9 Zeta potential plot for ACG2 nanocomposite in t-BuOH.

Table S5 Comparison of photodegradation of MB dye using different photocatalysts.

Sl. No	Photocatalyst	Irradiation Source	Pollutant Conc. (mg L^{-1})	Photocatalyst conc. (mg mL^{-1})	Time (min)	Degradation (%)	Year/ Ref.
1	ZnO-RGO	500 W UV lamp	5	15	250	92	(2011)[1]
2	GCN-S_5	400 W Halogen lamp	20	80	60	95	(2013)[2]
3	GCN-$BiVO_4$	300 W Xe lamp	10	100	90	95	(2014)[3]
4	CGN-TiO_2	100 W Halogen lamp	15	25	100	98	(2013)[4]
5	Cu-CGN	300 W Xe lamp	10	40	15	100	(2015)[5]
6	GCN-CdS	500 W Xe lamp	25	80	180	90	(2014)[6]
7	Au NST-GCN-RGO	90 W CFL bulb	20	15	135	92	This work

Table S6 Comparison of photodegradation of TC using different photocatalysts.

Sl. No.	Photocatalyst	Irradiation Source	Pollutant Conc. (mg L^{-1})	Photocatalyst conc. (mg mL^{-1})	Time (min)	Degradation (%)	Year/ Ref.
1	GCN-DM	500 W Xe Lamp	10	10	70	100	(2017)[7]
2	RGO/Cu_2O/Bi_2O_3	250 W Xe Lamp	10	50	180	75	(2017)[8]
3	AgI/$BiVO_4$	300 W Xe Lamp	20	30	60	95	(2016)[9]
4	Ca-CdSe/RGO	350 W Xe Lamp	15	50	60	82	(2015)[10]
5	Au/Pt/GCN	500 W Xe Lamp	20	100	180	93	(2015)[11]
6	Ag_3PO_4/Ag/$BiVO_4$/RGO	300 W Xe Lamp	10	50	60	95	(2017)[12]
7	Ag/Bi_3TaO_7	250 W Xe Lamp	10	50	120	85	(2015)[13]
8	Ag/Fe_3O_4/GCN	300 W Xe Lamp	20	50	90	88	(2016)[14]
9	GCN/ZnO/HNT	350 W Xe Lamp	20	100	60	87	(2015)[15]
10	Au NST-GCN-RGO	90 W CFL bulb	20	15	90	94	This work

Table S7 Comparison table for synthesis of 2-benzimidazole derivatives using different photocatalysts.

Sl. No.	Photocatalyst	Irradiation source	Time (min)	Yield (%)	Year/ Ref.
1	Pt@TiO_2 Nanoparticles	2 kW Xenon lamp	240	99	(2010)[16]
2	3,6-Disubstituted-s-Tetrazine	Visible light	120	90	(2013)[17]
3	MgI_2	Fluorescence lamp	360	97	(2014)[18]
4	CdSe/MMT	35 W Tungsten lamp	120	91	(2015)[19]
5	Rose Bengal	11 W LED bulb	120	90	(2016)[20]
6	NiO@anatase/rutile-TiO_2 nanoparticles	UV55W (UV-C) mercury lamp	-	98	(2017)[21]
7	Cd-ZnO nanoflakes	450 W Microwave irradiation	3.5	94	(2017)[22]
8	Bi_2WO_6	35 W Tungsten lamp	210	89	(2017)[23]
9	TiO_2/AA/Co	Visible light	180	90	(2018)[24]
10	fluorescein	10 W Blue LED	60	90	(2019)[25]
11	Au NST-GCN-RGO	45 W CFL bulb	360	92	This work

S2 Green chemistry matrices calculation

Green chemistry matrices calculations have been done for our developed catalytic reaction for the synthesis of benzimidazole derivatives. The following four parameters described below are important parameters for a Green or sustainable reaction.

(1) E-factor or environmental factor

(2) Atom economy (AE)

(3) Product mass intensity (PMI)

(4) Reaction mass efficiency (RME)

Green chemistry matrices calculations for compound 4a

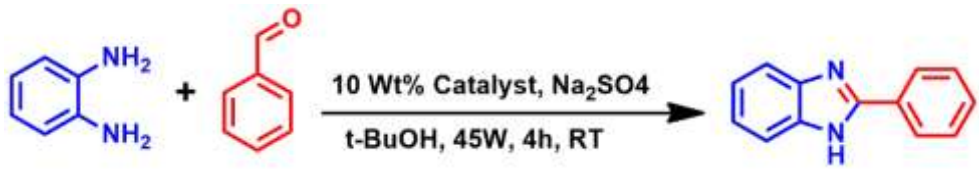

F.W. 108.14 g mol^{-1} 106.12 g mol^{-1} 287.31 g mol^{-1}

E-factor or environmental factor E-factor: Environmental-factor is a popular Green chemistry matrix which defines the ratio of mass of waste to mass of product.

E-factor = [mass of waste]/ mass of product

Mass of waste = Total mass of raw materials - Total mass of product (4a)

E- Factor = (108.14 mg +106.12 mg) – 185.23 mg / 180.23 mg (4a)

E- Factor = 0.156

Atom economy (AE): AE of a reaction describes the total number of atoms from the starting materials reside in the product. It is considered as a main matrix for efficiency of a reaction. The ideal value of AE factor is 100% (which means all atoms from the starting materials still resides in the product).

AE = Mol. wt. of product ÷ Σ(MW of stoichiometric reactants) × 100

$$AE = \frac{194.23}{108.14+106.12} *100$$

$$= 90.65\%$$

Product mass intensity (PMI): PMI is the total mass used in a chemical process divided by themass of product. In PMI solvent is also considered, hence tertiary butanol also adds value to PMI.

PMI = Σ(mass of stoichiometric reactants + solvent) / mass of product (4a)

$$PMI = \frac{214.26+74.12}{185.23}$$

$$= 1.556$$

Actual or ideal PMI = E-factor + 1

Hence, PMI = 0.156 + 1

= 1.156

Reaction mass efficiency (RME): Reaction mass efficiency is defined as the mass of product divided by the sum of total mass of stoichiometric reactants.

R.M.E. = mass of product /Σ(mass of stoichiometric reactants) × 100

$$\text{Reaction mass efficiency} = \frac{185.23}{108.14+106.12} * 100$$

$$= 86.45\%$$

RME measures the "cleanness" of a chemical reaction. Values of RME range from 0-100 %. Larger number is considered better for an ideal reaction.

S3 Compounds characterization

2-phenyl-1H-benzo[d]imidazole(4a)[26] Pale yellow solid, 85%; ^{1}H NMR (500 MHz, DMSO-d_6) δ (ppm) 12.95 (Br s, 1H), 8.17 (d, 2H, J=7.55 Hz), 7.62-7.59 (m, 2H), 7.57-7.55 (m, 2H), 7.54-7.48 (m, 1H). ^{13}C NMR (125 MHz, DMSO-d_6) δ (ppm) 160.3, 153.5, 148.4, 144.9, 142.1, 133.9, 129.4, 128.8, 123.9, 124.7, 117.0, 115.9, 115.0. HRMS, m/z [M+1] calculated for $C_{13}H_{11}N_2$, 195.0878; observed 195.0876.

2-(4-nitrophenyl)-1H-benzo[d]imidazole(4b)[27] light Yellow solid, 80%; ^{1}H NMR (500 MHz, DMSO-d_6) δ (ppm) 13.31 (Br s, 1H), 8.43 (m, 4H), 7.67 (m, 2H), 7.25 (m, 2H). ^{13}C NMR (125 MHz, DMSO-d_6) δ (ppm) 149.0, 147.8, 143.8, 136.0, 135.2, 127.4, 124.4, 123.6, 122.4, 119.5, 111.8. HRMS, m/z $[M]^+$ calculated for $C_{13}H_{11}N_2$, 238.1560; observed 238.120.

2-(4-chlorophenyl)-1H-benzo[d]imidazole(4c)[28] Light yellow solid, 82%; ^{1}H NMR (500 MHz, DMSO-d_6) δ (ppm) 12.99 (Br s, 1H), 8.20-8.17 (m, 2H), 7.66 (d, 1H, J=7.55 Hz), 7.64-7.61 (m, 2H), 7.53 (d, 1H, J=7.55 Hz), 7.24-7.18 (m, 2H). ^{13}C NMR (125 MHz, DMSO-d_6) δ (ppm) 150.1, 143.7, 135.0, 134.5, 129.1, 129.0, 128.1, 122.8, 121.8, 118.9, 111.4. HRMS, m/z $[M]^+$ calculated for $C_{13}H_{10}ClN_2$, 229.1095; observed 229.0509.

2-(p-tolyl)-1H-benzo[d]imidazole (4d)[27] Light yellow solid, 90%; ^{1}H NMR (500 MHz, DMSO-d_6) δ (ppm) 12.82 (Br s, 1H), 8.06 (d, 2H, J=8.25 Hz), 7.62-7.50 (m, 2H), 7.35 (d, 2H, J=8.25 Hz), 7.18 (d, 2H, J=4.85 Hz), 2.38 (s, 3H). ^{13}C NMR (125 MHz, DMSO-d_6) δ (ppm) 132.2, 130.8, 130.1, 129.2, 128.2, 126.8, 125.6, 29.7. HRMS, m/z [M+1] calculated for $C_{14}H_{13}N_2$, 208.1000; observed 209.1010.

2-(1H-benzo[d]imidazol-2-yl)-4-bromophenol(4e)[27] Yellow solid, 88%; ^{1}H NMR (500 MHz, DMSO-d_6) δ (ppm) 13.30 (Br s, 1H), 13.27 (Br s, 1H), 8.29 (d, 1H, J=2.75 Hz), 7.73 (d, 1H, J=7.55 Hz), 7.62 (d, 1H, J=8.25 Hz), 7.52 (dd, 1H, J=8.9 Hz, J=2.75 Hz), 7.32-7.26 (m, 2H), 7.02 (d, 1H, J=8.95 Hz) . ^{13}C NMR (125 MHz, DMSO-d_6) δ (ppm) 157.1, 150.3, 134.0, 128.5, 123.2, 119.5, 114.7, 110.2. HRMS, m/z [M] calculated for $C_{13}H_9BrON_2$, 289.1274; observed 289.0200 and, m/z $[M]^{2+}$ calculated for $C_{13}H_7BrON_2$ 287.9898; observed 287.0218.

phenyl(2-phenyl-1H-benzo[d]imidazol-5-yl)methanone(4f)[26] Yellow solid, 86%; ^{1}H NMR (500 MHz, DMSO-d_6) δ (ppm) 13.33 (Br s, 1H), 8.20 (d, 1H, J=6.85 Hz), 8.00-7.91 (m, 1H), 7.77 (d, 3H, J=6.85 Hz), 7.69-7.66 (m, 2H), 7.58 (m, 5H) . ^{13}C NMR (125 MHz, DMSO-d_6) δ (ppm) 154.5, 153.6, 143.1, 138.1, 132.3, 132.2, 131.4, 130.6, 129.5, 129.2, 128.5, 126.8, 124.7, 123.9, 121.7, 118.7, 114.2, 111.6. HRMS, m/z [M] calculated for $C_{13}H_9BrON_2$, 289.1274; observed 289.0200 and, m/z [M+1] calculated for $C_{20}H_{14}N_2O$ 299.1140; observed 299.1230.

S4 HRMS and NMR spectra of the compounds

^{1}H-NMR spectra of 2-phenyl-1H-benzo[d]imidazole

[500 MHz, DMSO-d_6]

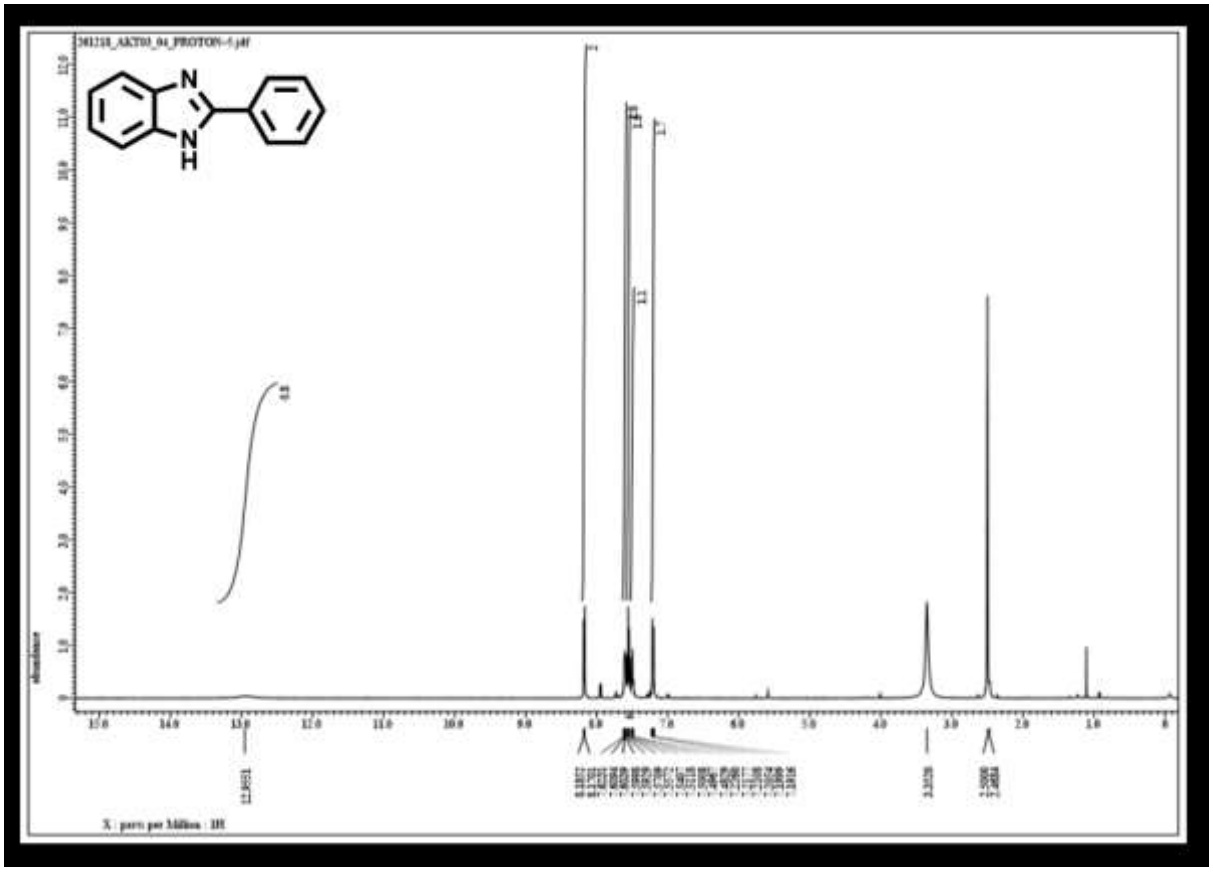

^{13}C-NMR spectra of 2-phenyl-1H-benzo[d]imidazole

[125 MHz, DMSO-d_6]

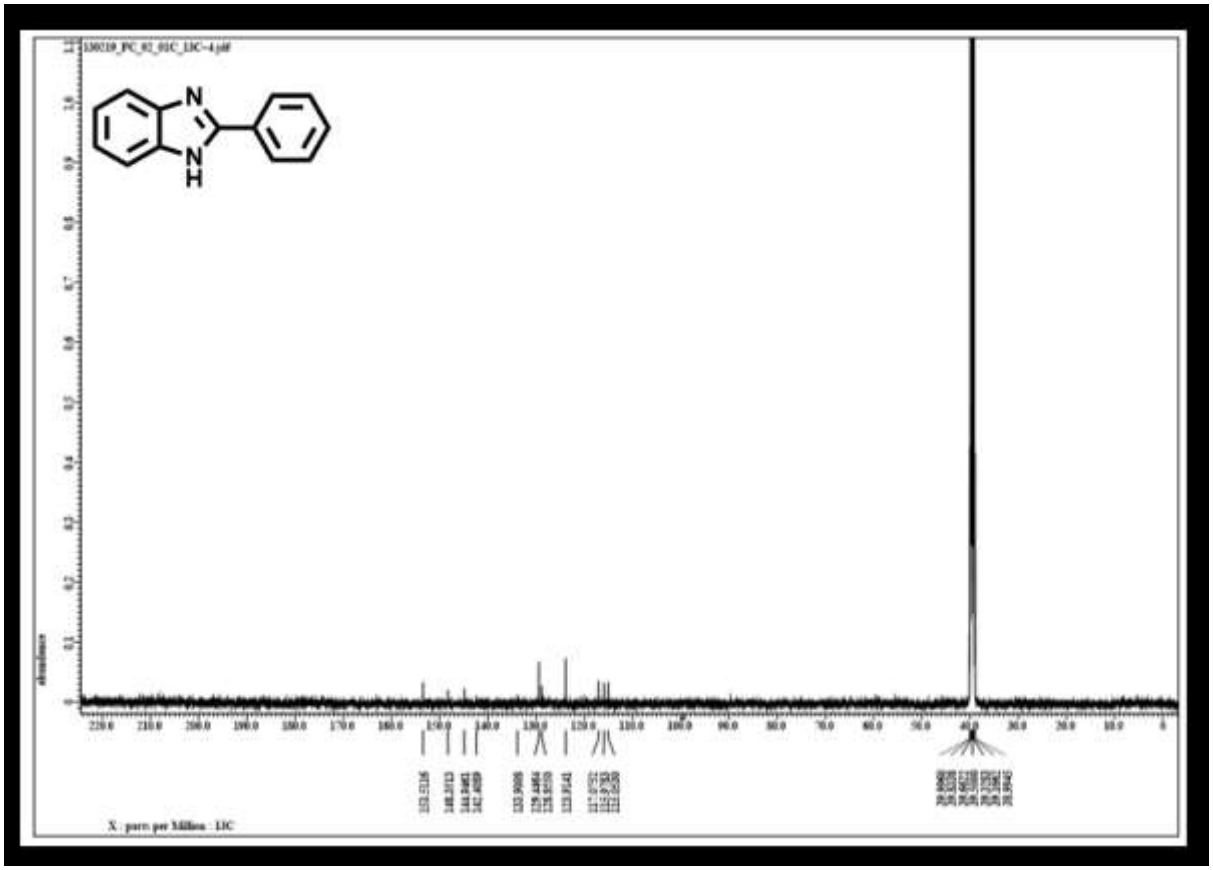

^{1}H-NMR spectra of 2-(4-nitrophenyl)-1H-benzo[d]imidazole

[500 MHz, DMSO-d_6]

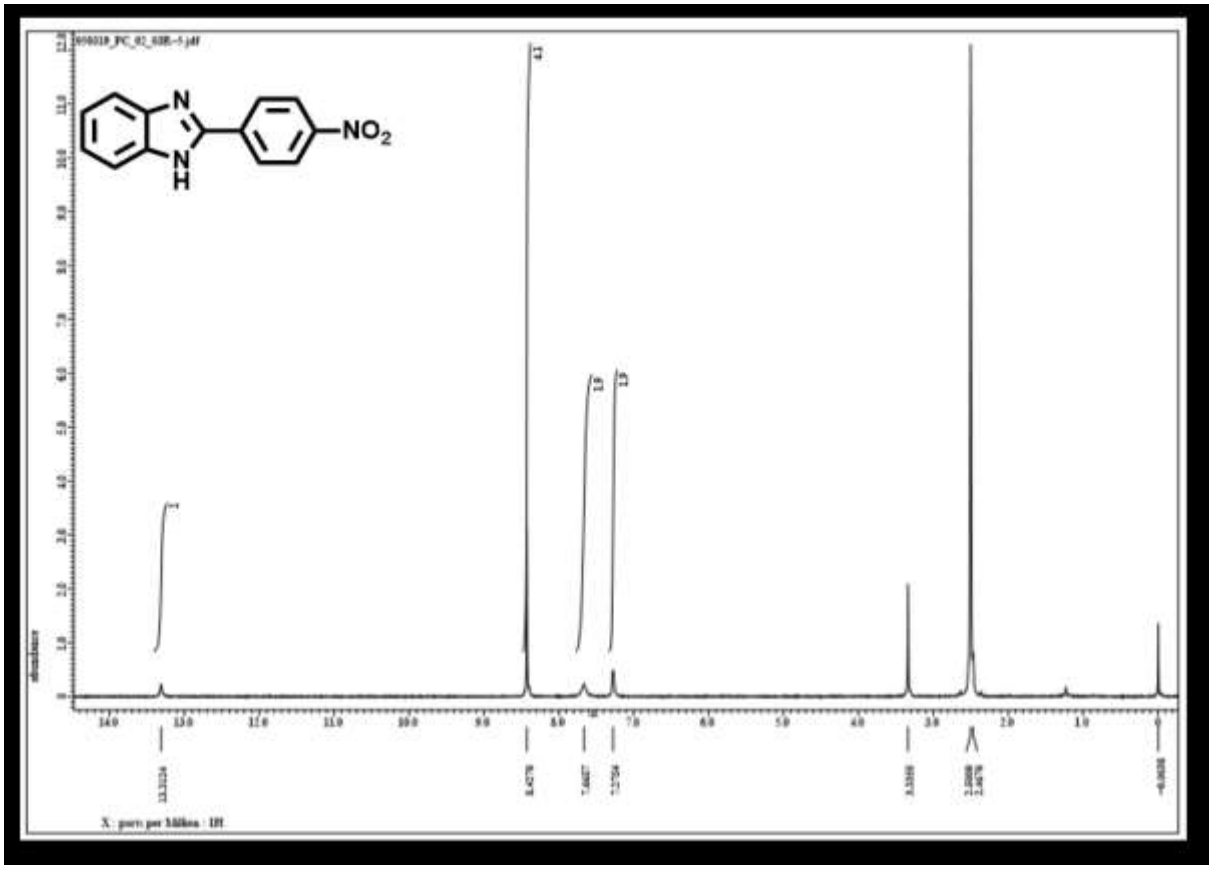

^{13}C-NMR spectra of 2-(4-nitrophenyl)-1H-benzo[d]imidazole

[125 MHz, DMSO-d_6]

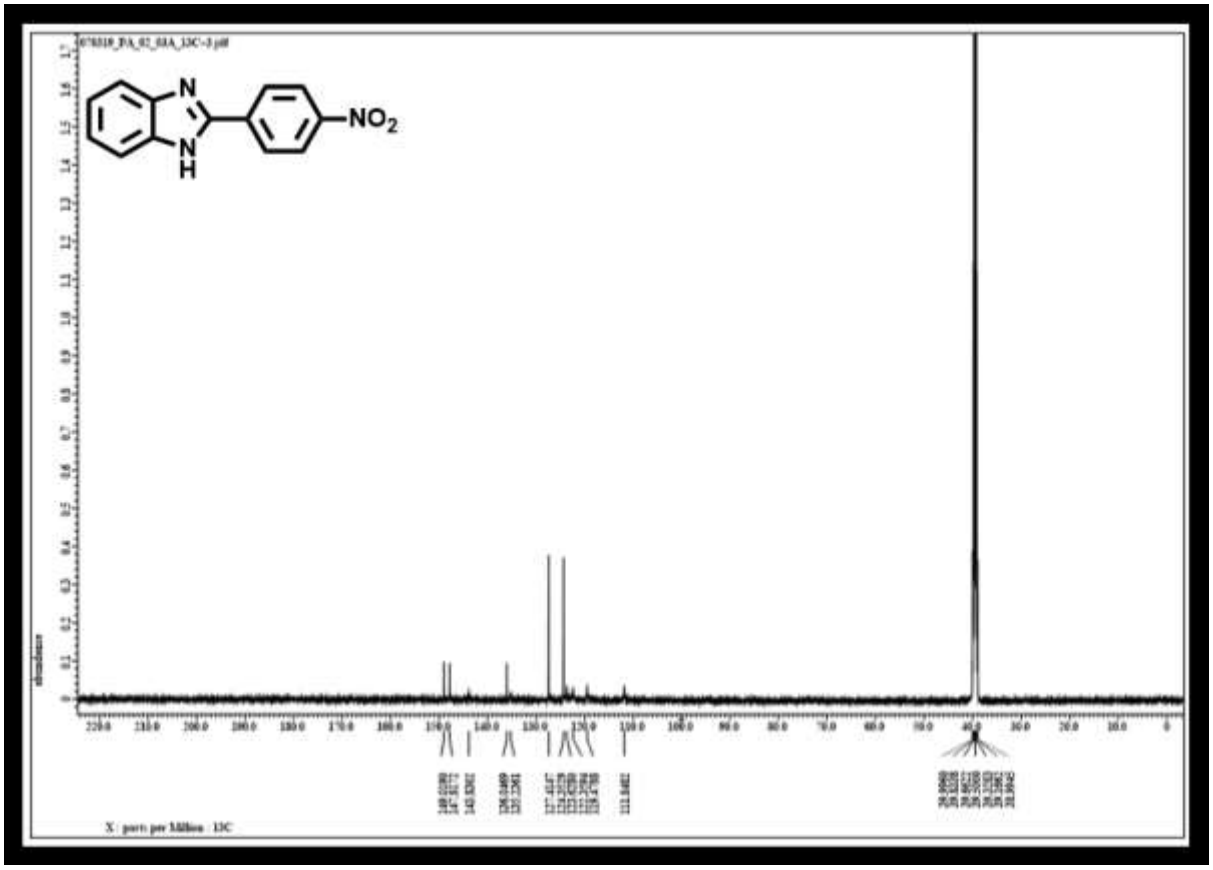

^{1}H-NMR spectra of 2-(4-chlorophenyl)-1H-benzo[d]imidazole

[500 MHz, DMSO-d_6]

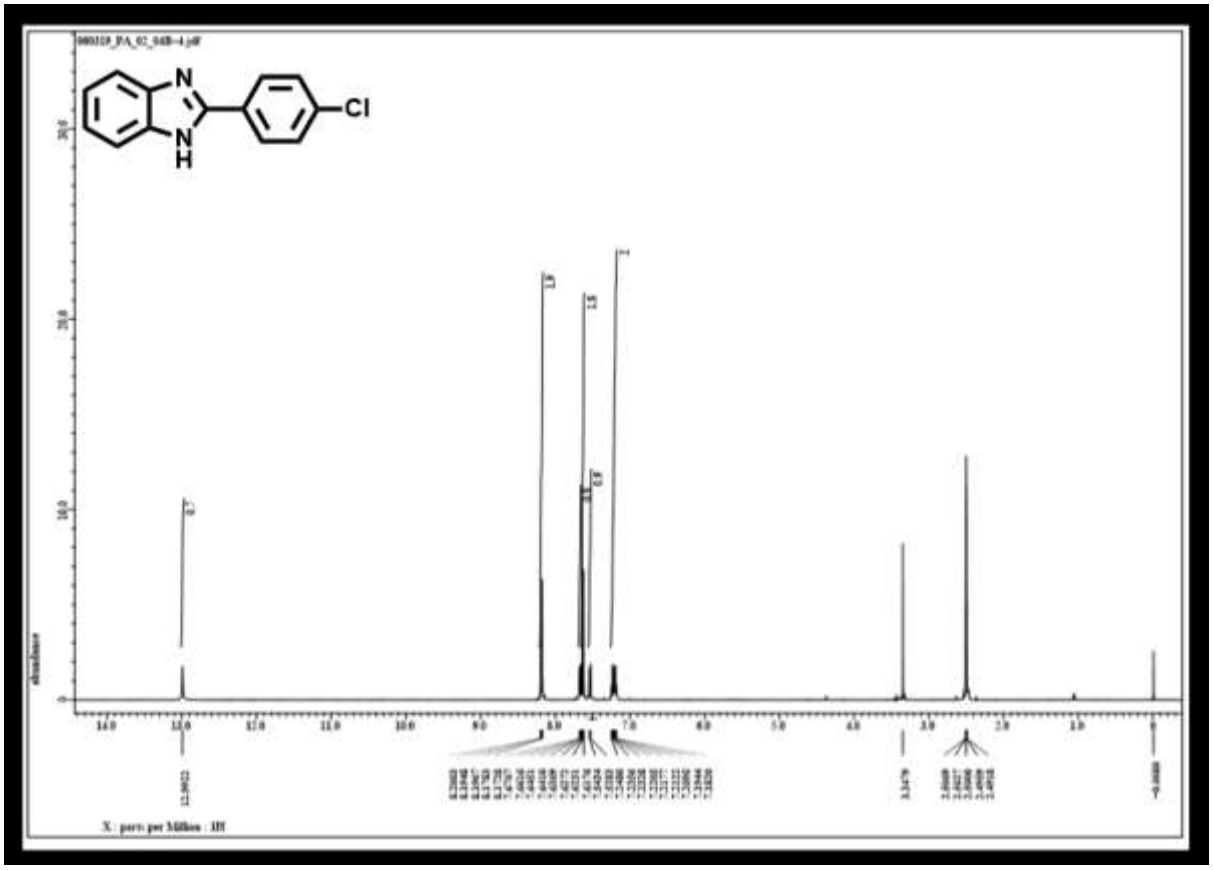

^{13}C-NMR spectra of 2-(4-chlorophenyl)-1H-benzo[d]imidazole

[125 MHz, DMSO-d_6]

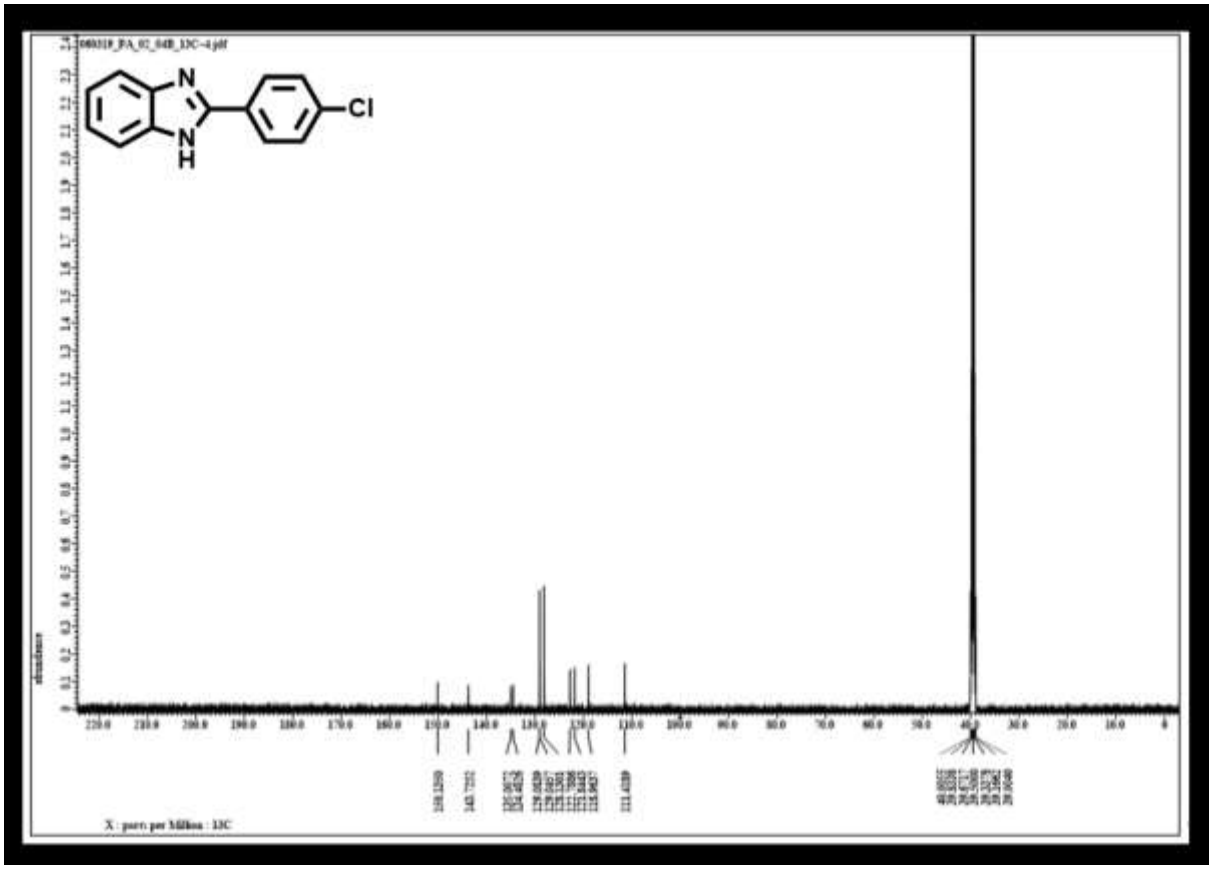

^{1}H-NMR spectra of 2-(p-tolyl)-1H-benzo[d]imidazole

[500 MHz, DMSO-d_6]

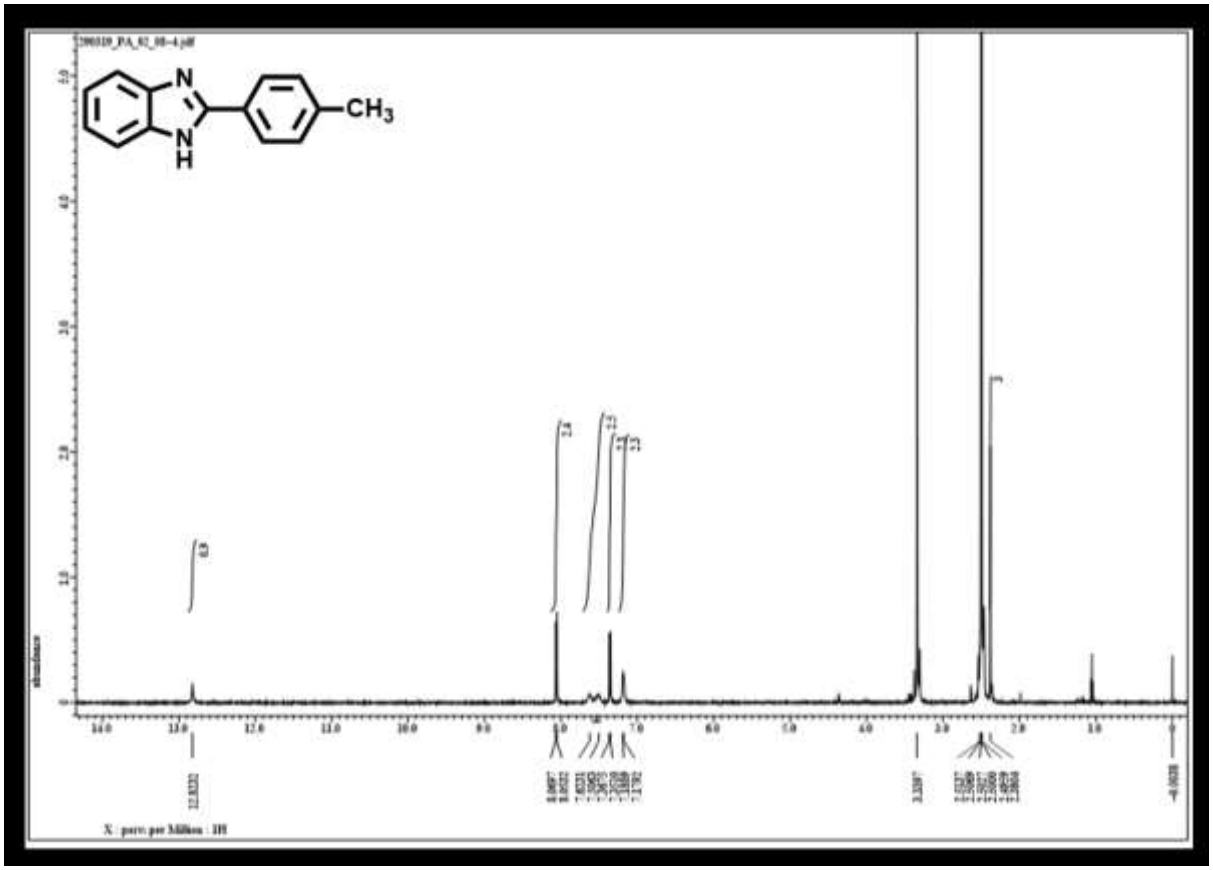

^{13}C-NMR spectra of 2-(p-tolyl)-1H-benzo[d]imidazole

[125 MHz, DMSO-d_6]

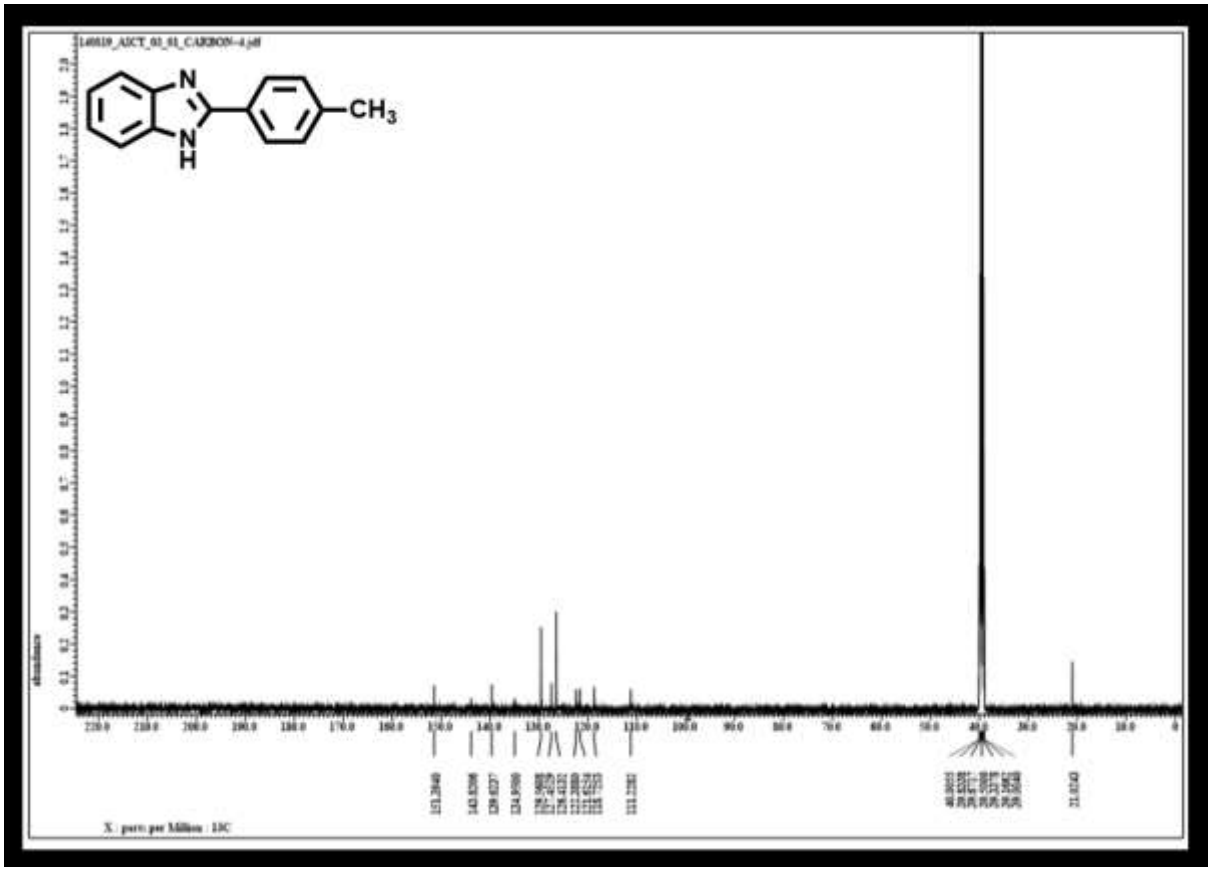

^{1}H-NMR spectra of 2-(1H-benzo[d]imidazol-2-yl)-4-bromophenol

[500 MHz, DMSO-d_6]

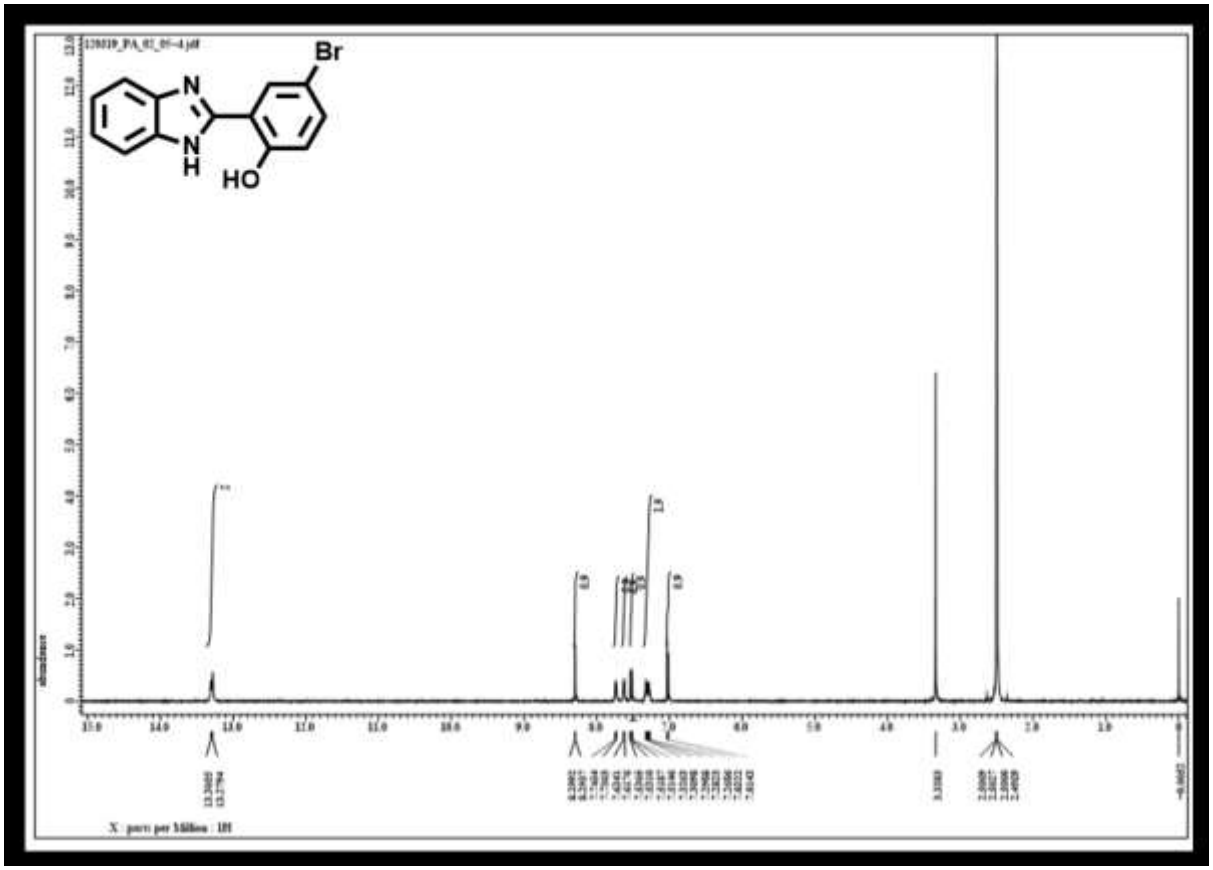

^{13}C-NMR spectra of 2-(1H-benzo[d]imidazol-2-yl)-4-bromophenol

[125 MHz, DMSO-d_6]

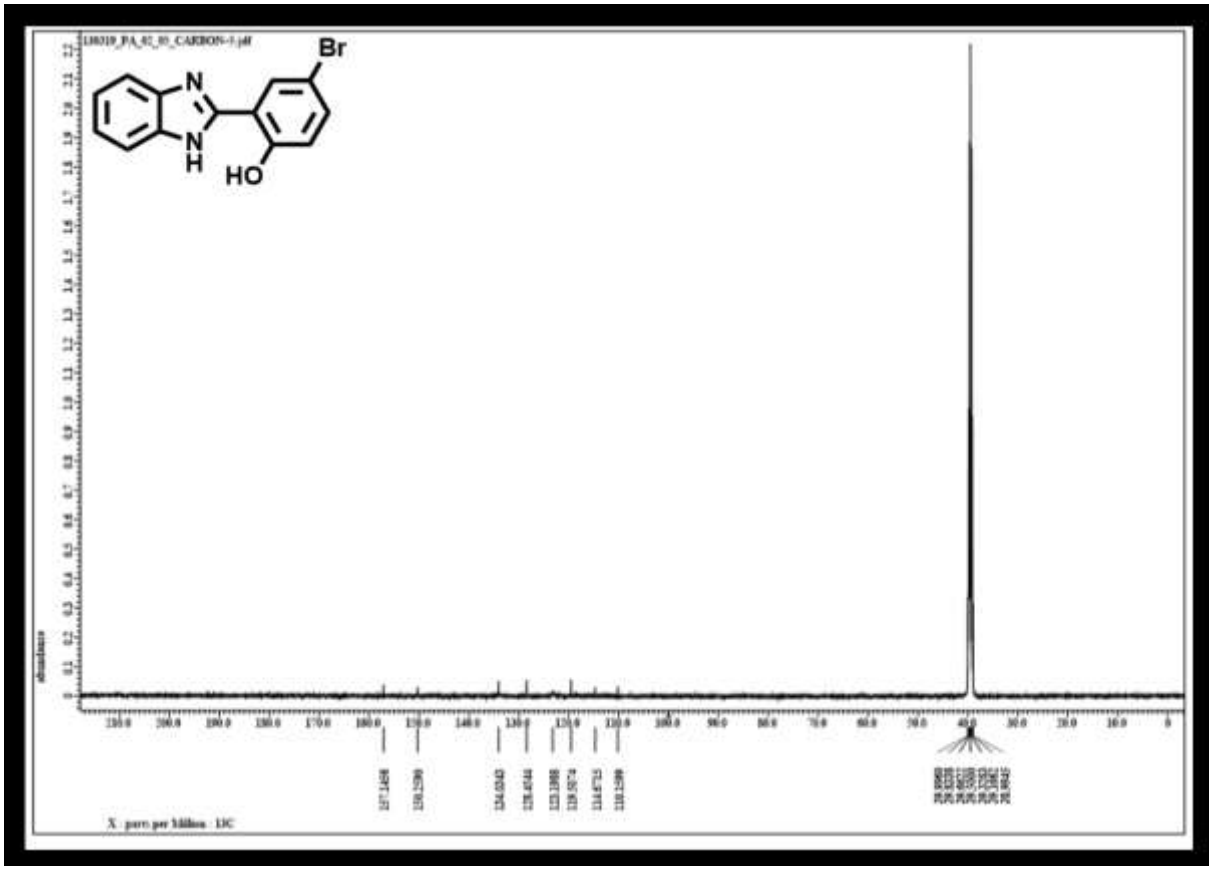

^{1}H-NMR spectra of phenyl(2-phenyl-1H-benzo[d]imidazol-5-yl)methanone

[500 MHz, DMSO-d_6]

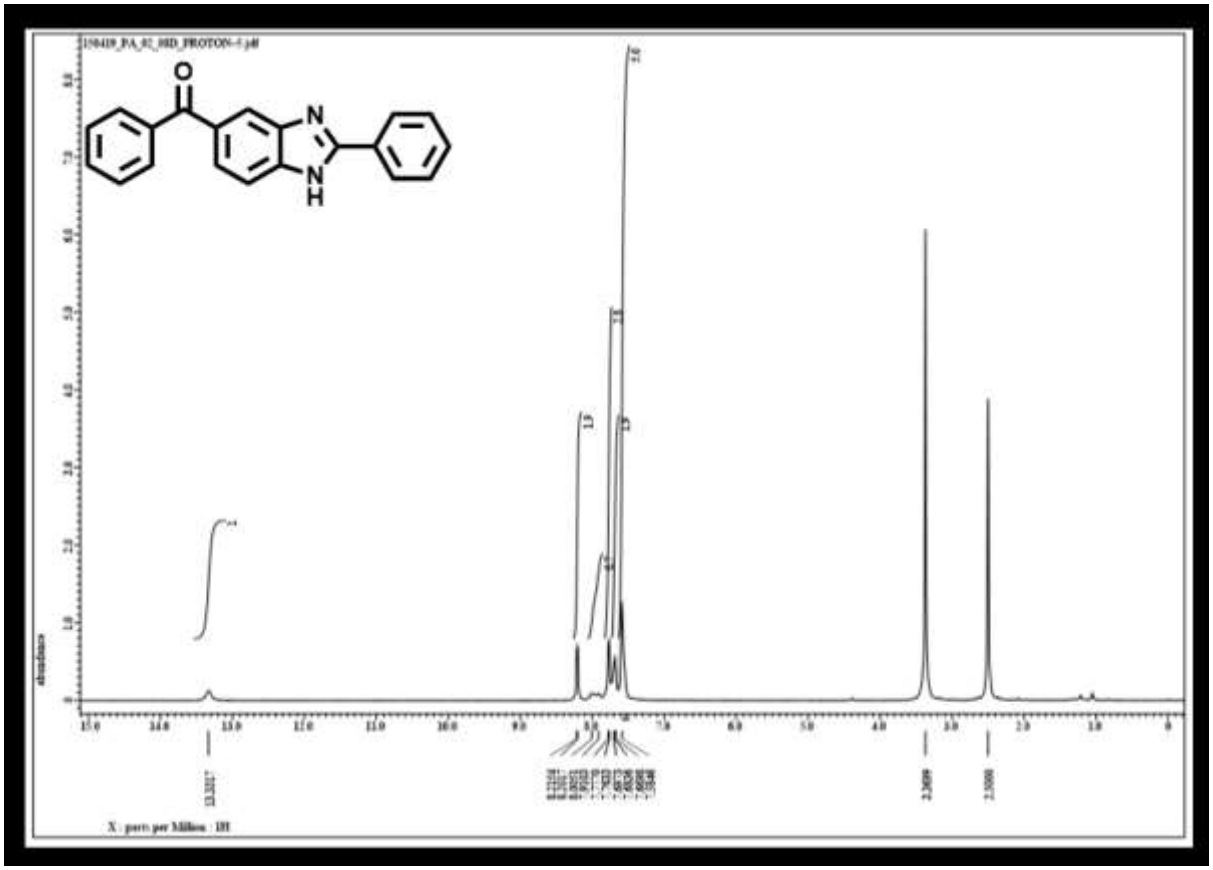

^{13}C-NMR spectra of phenyl(2-phenyl-1H-benzo[d]imidazol-5-yl)methanone

[125 MHz, DMSO-d_6]

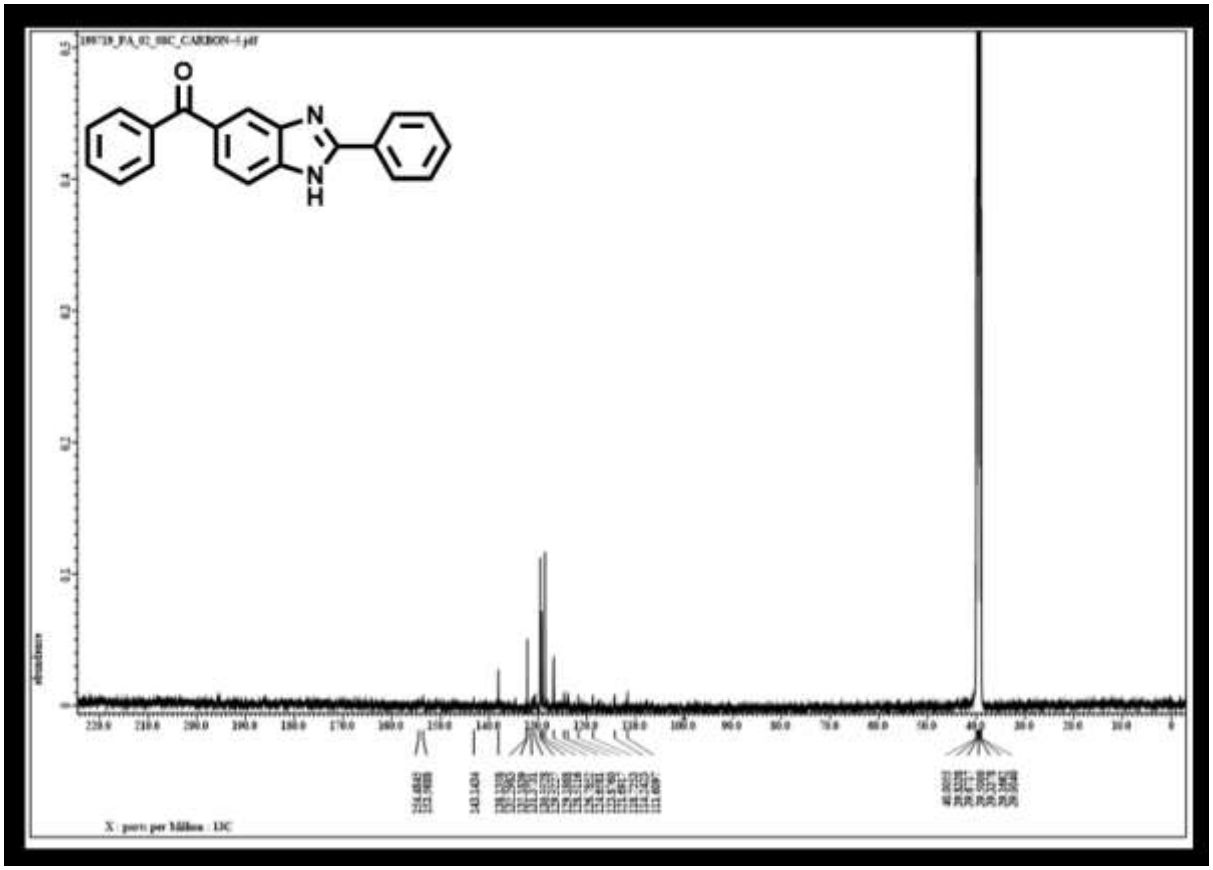

HRMS spectra of 2-phenyl-1H-benzo[d]imidazole

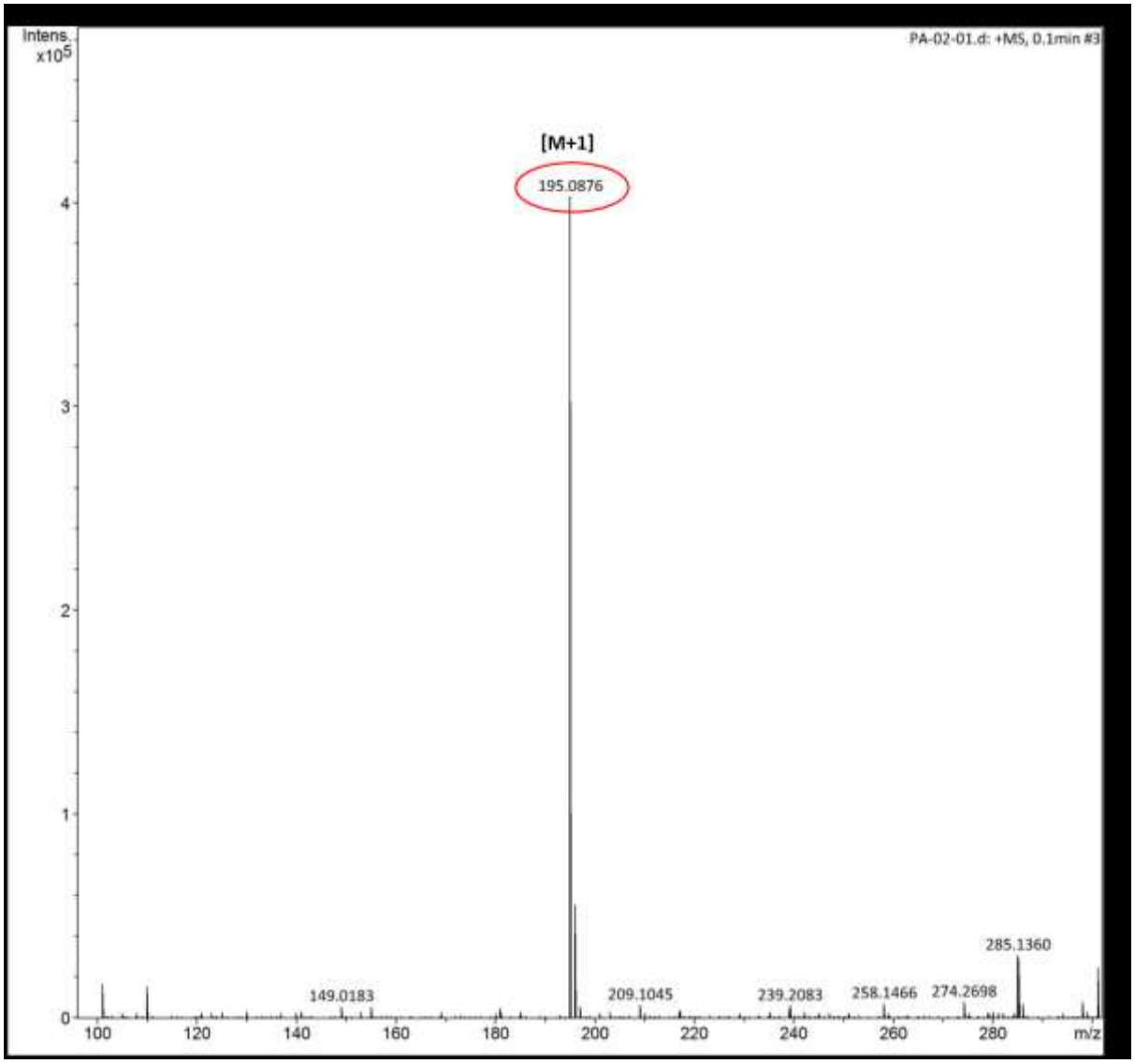

HRMS spectra of 2-(4-nitrophenyl)-1H-benzo[d]imidazole

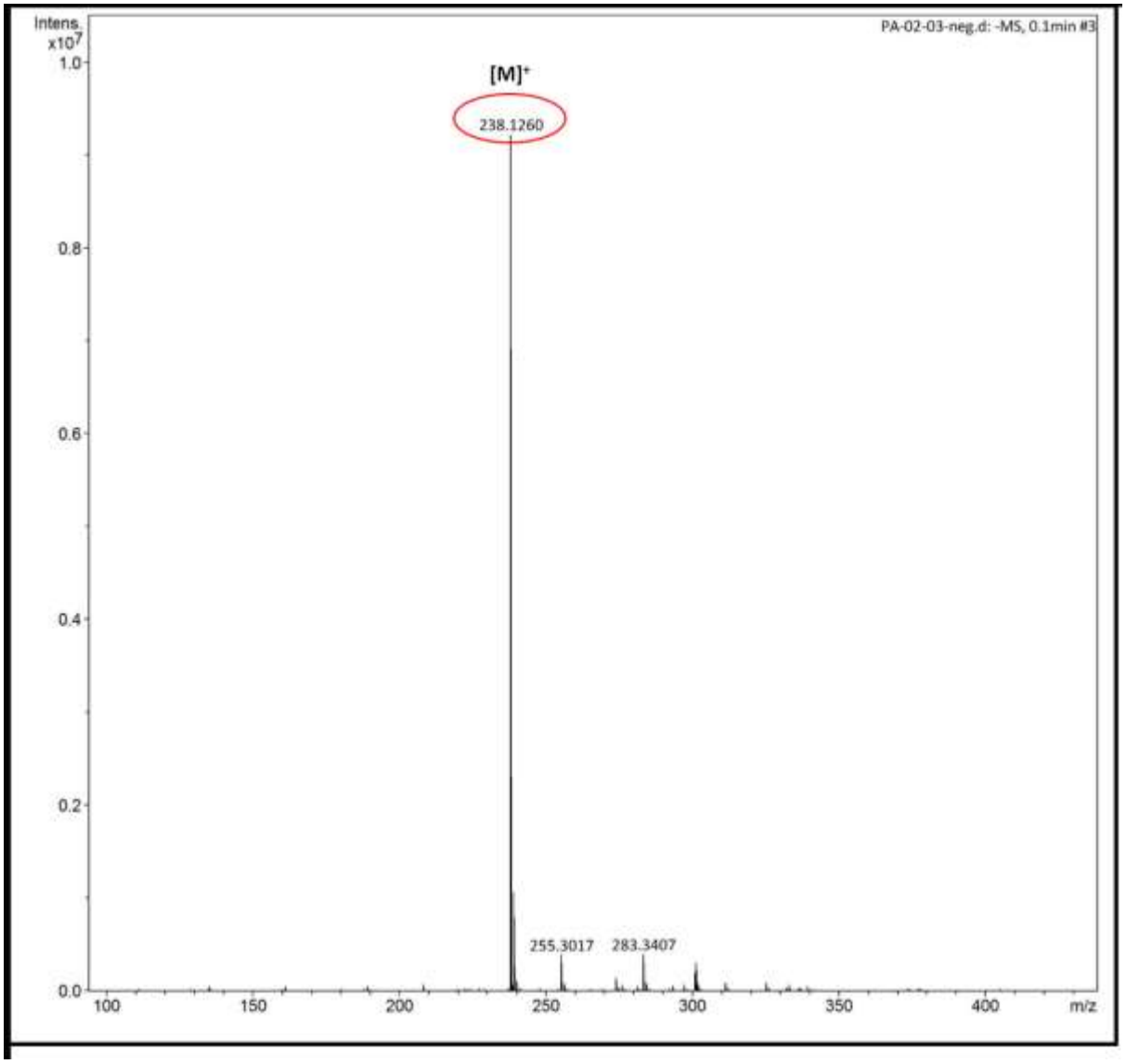

HRMS spectra of 2-(4-chlorophenyl)-1H-benzo[d]imidazole

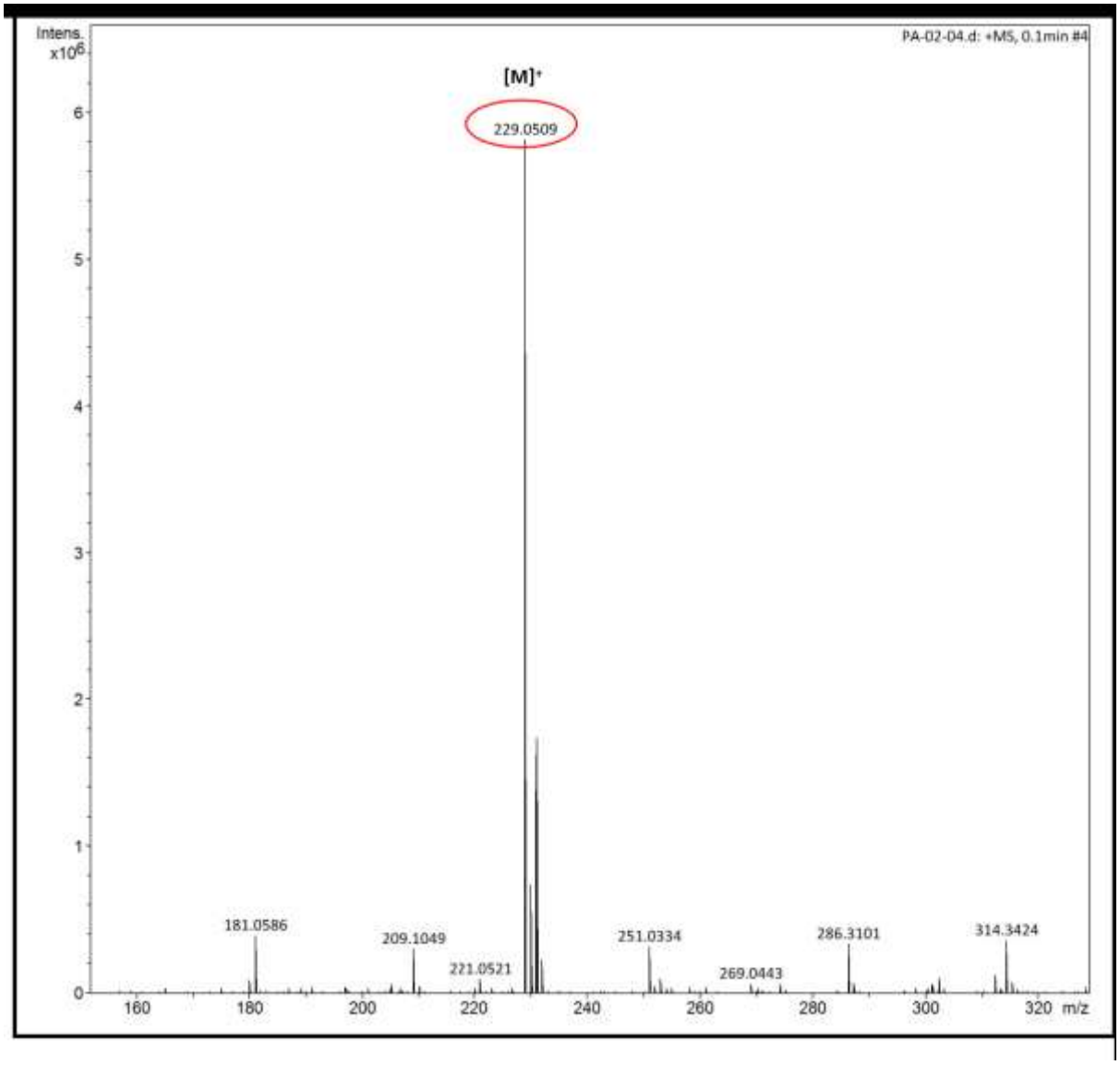

HRMS spectra of 2-(p-tolyl)-1H-benzo[d]imidazole

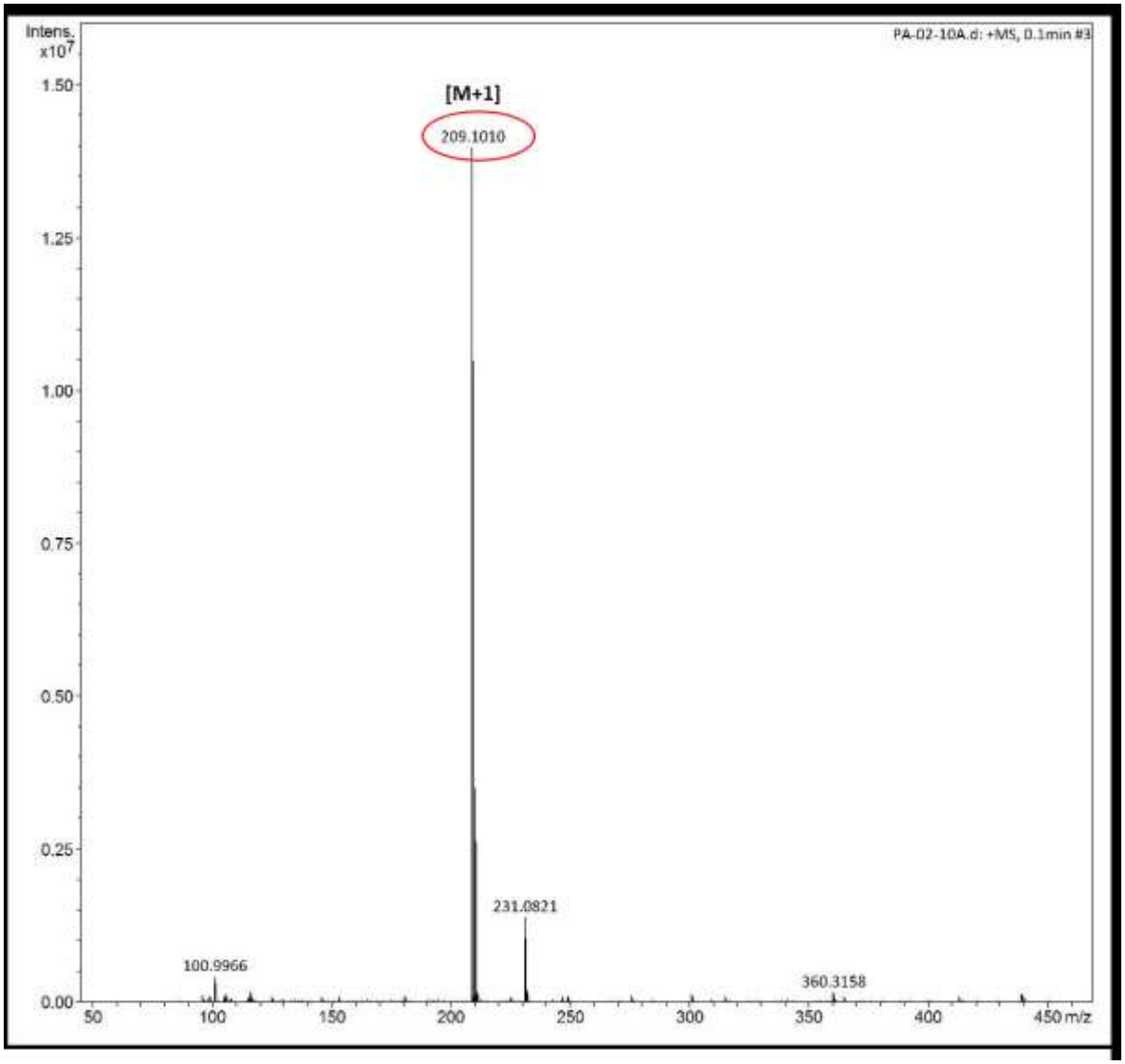

HRMS spectra of 2-(1H-benzo[d]imidazol-2-yl)-4-bromophenol

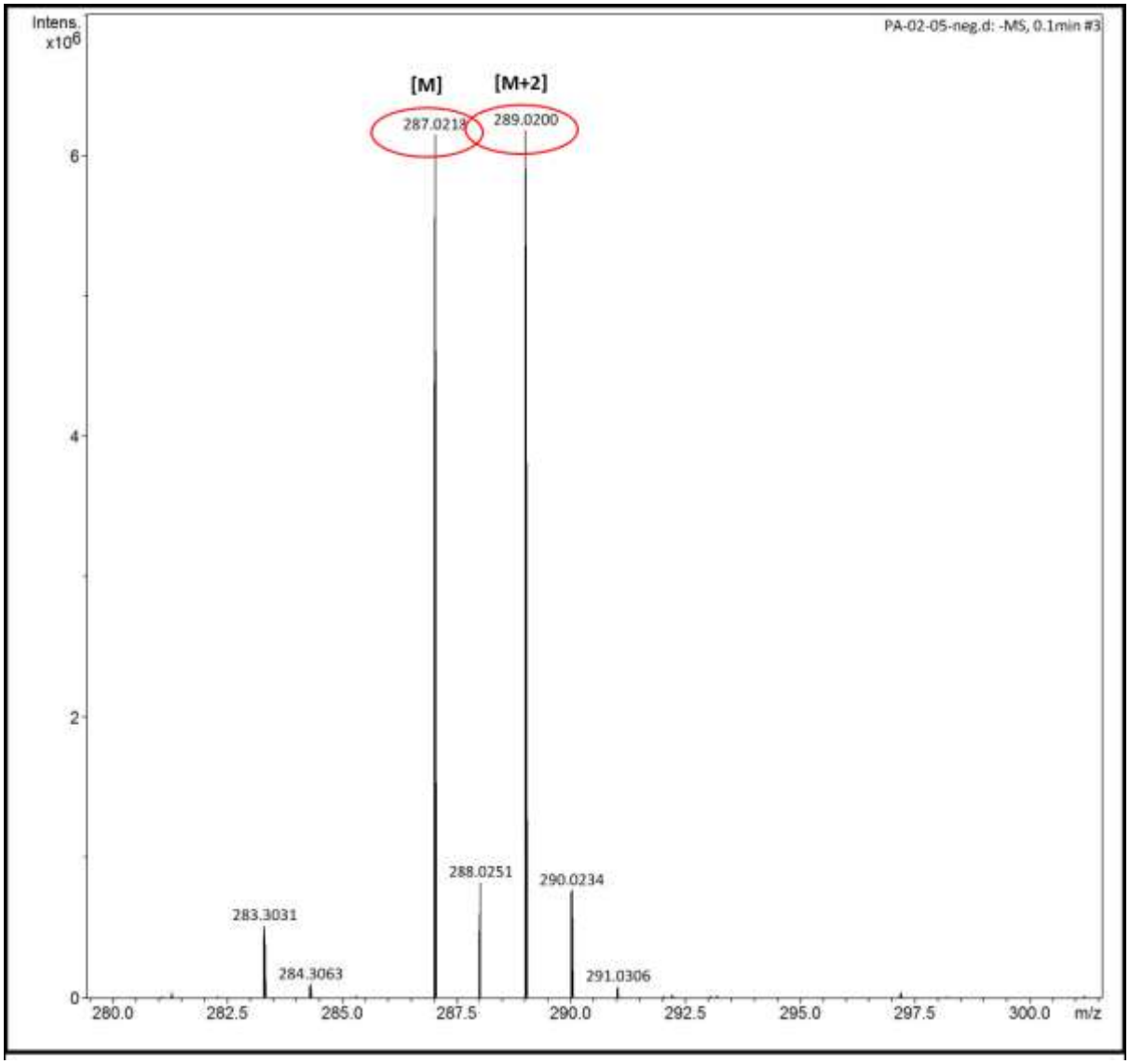

HRMS spectra of phenyl(2-phenyl-1H-benzo[d]imidazol-5-yl)methanone

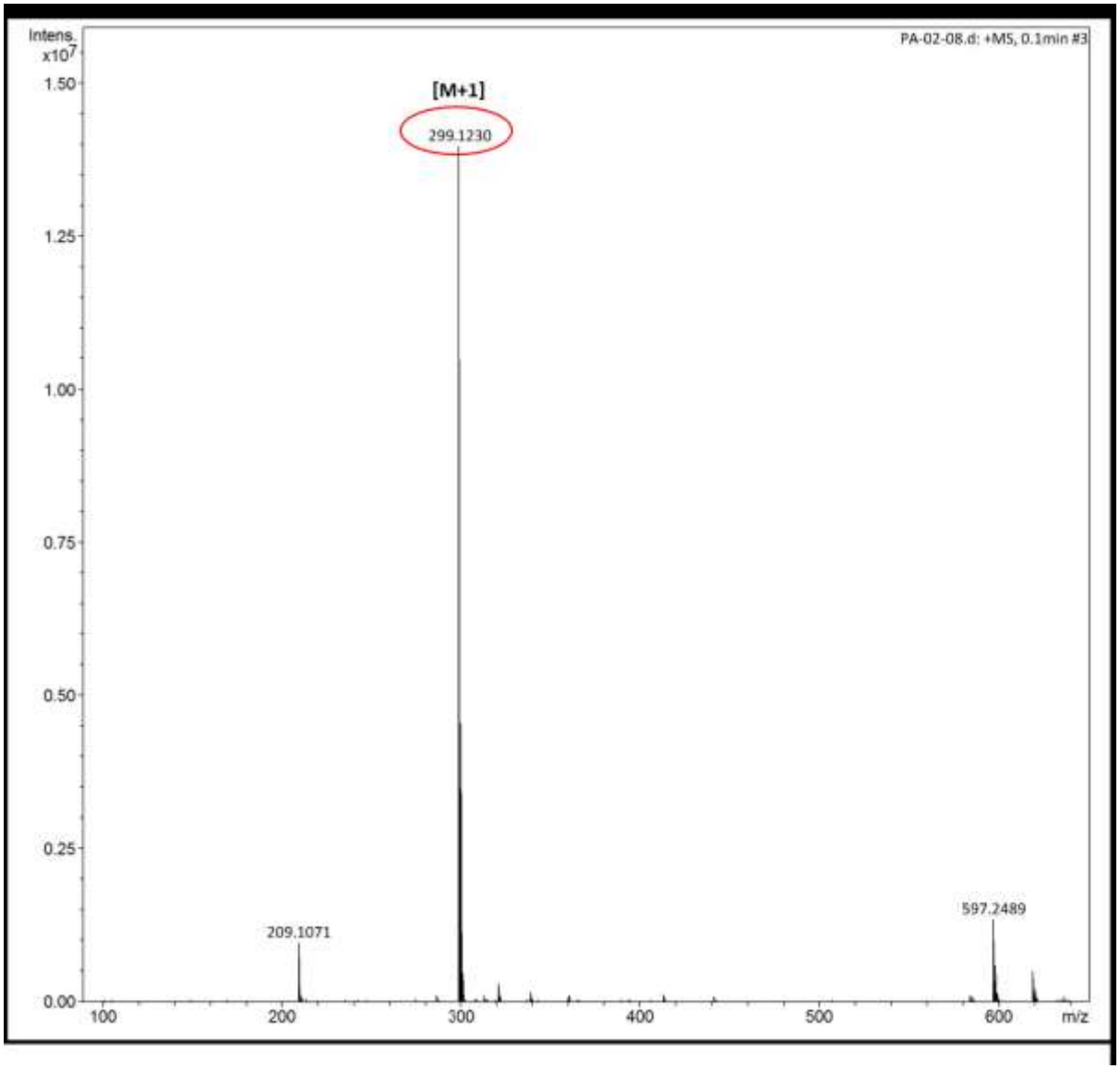

References

1. T. Lv, L. Pan, X. Liu, T. Lu, G. Zhu and Z. Sun, Enhanced photocatalytic degradation of methylene blue by ZnO-reduced graphene oxide composite synthesized via microwave-assisted reaction, *Journal of Alloys and Compounds*, 2011, **509**, 10086-10091.
2. F. Chang, Y. Xie, C. Li, J. Chen, J. Luo, X. Hu and J. Shen, A facile modification of g-C3N4 with enhanced photocatalytic activity for degradation of methylene blue, *Applied Surface Science*, 2013, **280**, 967-974.
3. Y. Tian, B. Chang, Z. Yang, B. Zhou, F. Xi and X. Dong, Graphitic carbon nitride–BiVO 4 heterojunctions: simple hydrothermal synthesis and high photocatalytic performances, *RSC Advances*, 2014, **4**, 4187-4193.
4. K. Sridharan, E. Jang and T. J. Park, Novel visible light active graphitic C3N4–TiO2 composite photocatalyst: Synergistic synthesis, growth and photocatalytic treatment of hazardous pollutants, *Applied Catalysis B: Environmental*, 2013, **142**, 718-728.
5. J. Gao, J. Wang, X. Qian, Y. Dong, H. Xu, R. Song, C. Yan, H. Zhu, Q. Zhong and G. Qian, One-pot synthesis of copper-doped graphitic carbon nitride nanosheet by heating Cu–melamine supramolecular network and its enhanced visible-light-driven photocatalysis, *Journal of Solid State Chemistry*, 2015, **228**, 60-64.
6. F. Jiang, T. Yan, H. Chen, A. Sun, C. Xu and X. Wang, A g-C3N4–CdS composite catalyst with high visible-light-driven catalytic activity and photostability for methylene blue degradation, *Applied Surface Science*, 2014, **295**, 164-172.
7. T. Muhmood, M. A. Khan, M. Xia, W. Lei, F. Wang and Y. Ouyang, Enhanced photo-electrochemical, photo-degradation and charge separation ability of graphitic carbon nitride (g-C3N4) by self-type metal free heterojunction formation for antibiotic degradation, *Journal of Photochemistry and Photobiology A: Chemistry*, 2017, **348**, 118-124.
8. H. Shen, J. Wang, J. Jiang, B. Luo, B. Mao and W. Shi, All-solid-state Z-scheme system of RGO-Cu2O/Bi2O3 for tetracycline degradation under visible-light irradiation, *Chemical Engineering Journal*, 2017, **313**, 508-517.
9. F. Chen, Q. Yang, J. Sun, F. Yao, S. Wang, Y. Wang, X. Wang, X. Li, C. Niu and D. Wang, Enhanced photocatalytic degradation of tetracycline by AgI/BiVO4 heterojunction

under visible-light irradiation: mineralization efficiency and mechanism, *ACS applied materials & interfaces*, 2016, **8**, 32887-32900.

10. M. Zhou, D. Han, X. Liu, C. Ma, H. Wang, Y. Tang, P. Huo, W. Shi, Y. Yan and J. Yang, Enhanced visible light photocatalytic activity of alkaline earth metal ions-doped CdSe/rGO photocatalysts synthesized by hydrothermal method, *Applied Catalysis B: Environmental*, 2015, **172**, 174-184.
11. J. Xue, S. Ma, Y. Zhou, Z. Zhang and M. He, Facile photochemical synthesis of Au/Pt/g-C3N4 with plasmon-enhanced photocatalytic activity for antibiotic degradation, *ACS applied materials & interfaces*, 2015, **7**, 9630-9637.
12. F. Chen, Q. Yang, X. Li, G. Zeng, D. Wang, C. Niu, J. Zhao, H. An, T. Xie and Y. Deng, Hierarchical assembly of graphene-bridged Ag3PO4/Ag/BiVO4 (040) Z-scheme photocatalyst: An efficient, sustainable and heterogeneous catalyst with enhanced visible-light photoactivity towards tetracycline degradation under visible light irradiation, *Applied Catalysis B: Environmental*, 2017, **200**, 330-342.
13. B. Luo, D. Xu, D. Li, G. Wu, M. Wu, W. Shi and M. Chen, Fabrication of a Ag/Bi3TaO7 plasmonic photocatalyst with enhanced photocatalytic activity for degradation of tetracycline, *ACS applied materials & interfaces*, 2015, **7**, 17061-17069.
14. Z. Zhu, Z. Lu, D. Wang, X. Tang, Y. Yan, W. Shi, Y. Wang, N. Gao, X. Yao and H. Dong, Construction of high-dispersed Ag/Fe3O4/g-C3N4 photocatalyst by selective photo-deposition and improved photocatalytic activity, *Applied Catalysis B: Environmental*, 2016, **182**, 115-122.
15. J. Li, M. Zhou, Z. Ye, H. Wang, C. Ma, P. Huo and Y. Yan, Enhanced photocatalytic activity of gC 3 N 4–ZnO/HNT composite heterostructure photocatalysts for degradation of tetracycline under visible light irradiation, *RSC Advances*, 2015, **5**, 91177-91189.
16. Y. Shiraishi, Y. Sugano, S. Tanaka and T. Hirai, One-Pot Synthesis of Benzimidazoles by Simultaneous Photocatalytic and Catalytic Reactions on Pt@ TiO2 Nanoparticles, *Angewandte Chemie International Edition*, 2010, **49**, 1656-1660.
17. S. Samanta, S. Das and P. Biswas, Photocatalysis by 3, 6-disubstituted-s-tetrazine: visible-light driven metal-free green synthesis of 2-substituted benzimidazole and benzothiazole, *The Journal of organic chemistry*, 2013, **78**, 11184-11193.

18. Y. Nagasawa, Y. Matsusaki, T. Hotta, T. Nobuta, N. Tada, T. Miura and A. Itoh, Aerobic photooxidative synthesis of benzimidazoles from aromatic aldehydes and diamines using catalytic amounts of magnesium iodide, *Tetrahedron Letters*, 2014, **55**, 6543-6546.

19. A. R. Wade, H. R. Pawar, M. V. Biware and R. C. Chikate, Synergism in semiconducting nanocomposites: visible light photocatalysis towards the formation of C–S and C–N bonds, *Green Chemistry*, 2015, **17**, 3879-3888.

20. J. Kovvuri, B. Nagaraju, A. Kamal and A. K. Srivastava, An Efficient Synthesis of 2-substituted benzimidazoles via photocatalytic condensation of o-phenylenediamines and aldehydes, *ACS combinatorial science*, 2016, **18**, 644-650.

21. A. Ziarati, A. Badiei, G. M. Ziarani and H. Eskandarloo, Simultaneous photocatalytic and catalytic activity of p–n junction NiO@ anatase/rutile-TiO2 as a noble-metal free reusable nanoparticle for synthesis of organic compounds, *Catalysis Communications*, 2017, **95**, 77-82.

22. S. P. Kunde, K. G. Kanade, B. K. Karale, H. N. Akolkar, P. V. Randhavane and S. T. Shinde, Effect of Cd-doping on the catalytic activity of ZnO nanoflakes in the synthesis of benzimidazoles, *Research on Chemical Intermediates*, 2017, **43**, 7277-7290.

23. A. P. Jakhade, M. V. Biware and R. C. Chikate, Two-Dimensional Bi2WO6 nanosheets as a robust catalyst toward photocyclization, *ACS omega*, 2017, **2**, 7219-7229.

24. F. Feizpour, M. Jafarpour and A. Rezaeifard, A tandem aerobic photocatalytic synthesis of benzimidazoles by cobalt ascorbic acid complex coated on TiO 2 nanoparticles under visible light, *Catalysis Letters*, 2018, **148**, 30-40.

25. Z. Li, H. Song, R. Guo, M. Zuo, C. Hou, S. Sun, X. He, Z. Sun and W. Chu, Visible-light-induced condensation cyclization to synthesize benzimidazoles using fluorescein as a photocatalyst, *Green chemistry*, 2019, **21**, 3602-3605.

26. H. Kaur, M. Venkateswarulu, S. Kumar, V. Krishnan and R. R. Koner, A metal–organic framework based multifunctional catalytic platform for organic transformation and environmental remediation, *Dalton Transactions*, 2018, **47**, 1488-1497.

27. Y.-S. Lee, Y.-H. Cho, S. Lee, J.-K. Bin, J. Yang, G. Chae and C.-H. Cheon, Significant facilitation of metal-free aerobic oxidative cyclization of imines with water in synthesis of benzimidazoles, *Tetrahedron*, 2015, **71**, 532-538.

28. M. Karthik and P. Suresh, Brønsted acidic reduced graphene oxide as a sustainable carbocatalyst: a selective method for the synthesis of C-2-substituted benzimidazole, *New Journal of Chemistry*, 2018, **42**, 17931-17938.